1-1-2007

A diffusion model of lightning radiative transfer using cylindrical geometry

Rina Alfonso Santos
University of Nevada, Las Vegas

Repository Citation

Santos, Rina Alfonso, "A diffusion model of lightning radiative transfer using cylindrical geometry" (2007). *UNLV Retrospective Theses & Dissertations*. 2262.
http://dx.doi.org/10.25669/5ecp-c5ea

A DIFFUSION MODEL OF LIGHTNING RADIATIVE TRANSFER USING CYLINDRICAL GEOMETRY

by

Rina Alfonso Santos

Associate of Science
College of Alameda, California
1986

Bachelor of Science
California State University, Hayward
1993

A thesis submitted in partial fulfillment
of the requirements for the

Master of Science Degree in Mathematical Sciences
Department of Mathematical Sciences
College of Sciences

Graduate College
University of Nevada, Las Vegas
December 2007

ProQuest LLC
789 E. Eisenhower Parkway
PO Box 1346
Ann Arbor, MI 48106-1346

UNLV
UNIVERSITY OF NEVADA LAS VEGAS

Thesis Approval

The Graduate College
University of Nevada, Las Vegas

11/16, 2007

The Thesis prepared by

Rina A. Santos

Entitled

A Diffusion Model of Lightning Radiative Transfer Using Cylindrical Geometry.

is approved in partial fulfillment of the requirements for the degree of

Master of Science in Mathematical Sciences

Examination Committee Chair

Dean of the Graduate College

Examination Committee Member

Examination Committee Member

Graduate College Faculty Representative

ABSTRACT

A Diffusion Model of Lightning Radiative Transfer Using Cylindrical Geometry

by

Rina Alfonso Santos

Dr. Dieudonne Phanord, Examination Committee Chair
Founding Director of the Center of Atmospheric, Oceanic & Space Sciences
Professor of Mathematics
University of Nevada, Las Vegas

Clouds come in different shapes and sizes and are made up of different constituents. Realistic clouds are composed of heterogeneous distribution of constituents (ice particle, needle shaped objects, cubic, hexagonal, etc.). For tractability of solutions and smoothness of calculations, assumptions are made. The assumption is viable due to multiple scattering effect for propagation of radiation in random media. In Koshak et al. (1994), "Diffusion Model for Lightning Radiative Transfer", the cloud was treated as a nuclear reactor in order to obtain forms that can be readily computable and a simple geometry was chosen, i.e., a homogeneous rectangular parallelepiped cloud. In a recent work by Odei (2007), the cloud was modeled by a sphere containing a homogeneous distribution of identical spherical water droplets. This research activity will focus on modeling lightning intensity inside a cylindrical cloud. In addition, the known analytical solution generated by the cylindrical model is simulated and graphically represented. Moreover, the results of this thesis are compared to the above cited references.

TABLE OF CONTENTS

LIST OF FIGURES

LIST OF TABLES

ACKNOWLEDGEMENTS

First and foremost, I would like to thank the Lord, Jesus Christ, my Savior, Son of the Almighty God, for without Him, this paper and all my studies could have never been accomplished. "I can do all things through Christ who strengthens me." (Philippians 4:11) I would also like to thank my husband, Raymond, for believing in me, encouraging me and loving me for 17 years. I could love no other man more than I love you. To my four children, Lorayna, Jordan, Gabriella and Joshua, thank you for being so good, respectful and loving. I love each one of you very much and each one of you I know will grow up to be a great man or woman of God that I am already proud of. Keep reading the Bible and stay close to God. I would also like to thank my dad and mom for helping me become the woman I am today. Daddy, you showed me how to be hard working and firm in discipline and Mommy, I could have never shown love and kindness to others without learning it from you first. I would like to thank my in-laws, Reynaldo and Carmelita (Pop and Mom), for helping me with the kids in my last years of school. I could have never finished without knowing that my kids were being loved and taken care of so well while I was in school. I will take care of both of you always. At College of Alameda, I would like to thank Dr. Michael Payne for his first inspiring me to become a math teacher. I enjoyed Calculus so much that I could think of no other profession to aspire to. At UNLV, I would like to first thank Dr. Dieudonne Phanord, my advisor and mentor for believing in me, encouraging me to finish (...hang in there!) and teaching me

the methods to accomplish this paper. You also taught me that even through the toughest of trials, your faith in God was unshaken. I have the utmost respect for you sir. I would like to thank Dr. Dennis Murphy for his support, especially pick up and drop off at the airport during my last semester, which truly shows that you are a dedicated friend. I would like to thank James Odei for studying with me and always being there for me in my toughest trials. You are a life-long friend. Thank you also to Hanamathu Rao Chava for his expertise in programming and work on the graphs. I would also like to thank all my professors at UNLV for all their knowledge and insight into the world of mathematics. I do aspire to your level of intelligence. I especially would like to thank those professors who agreed to be on my Advisory Committee, Dr. Zhonghai Ding, Dr. Rohan Dalpatadu and Dr. Michael Pravica. Thank you for your extra time and effort. I would also like to thank the secretaries for their support in all our paperwork as teachers and as students. Lastly, I would like to thank all my friends at UNLV for making it so much fun to come to class and learn from your questions also. I have truly grown from my academic and life experience here at UNLV and I will carry this knowledge and expertise into future endeavors with great pride.

CHAPTER 1

INTRODUCTION

The study of weather patterns is more relevant than ever because of its effects on people and ecosystems. Particularly important are cyclonic events such as tornadoes and hurricanes, along with their associated components such as cloud formation, lightning and precipitation. The importance of forecasting such events was seen in 2005 from the Category 5 hurricanes Katrina, Rita and Wilma. These hurricanes started in the Atlantic Ocean and moved inland towards Florida and Louisiana, causing great destruction. Forecasting systems and emergency procedures were relied upon for their accuracy and ability to save lives. The work to follow is a study of the initial stages of a hurricane, particularly cloud formation and lightning intensity. The chosen shape of the cloud is a cylinder. Lightning intensity models based on a cylindrical cloud using a diffusion technique developed in [1] will be compared to results obtained earlier for the parallelepiped [1] and spherically shaped cloud [2].

Mathematical modeling of intensity in a cloud requires many factors: the shape of the cloud, its assumed properties, approximations that will lead to analytical solutions that can be simulated for graphical representation, and the physical laws that govern cloud dynamics. The seminal study [1] in this area used a parallelepiped cloud shape. Description of its intensity dynamics is summarized in Chapter 3. A recent work [2] considered intensity in a spherical cloud. The results are similar to that of the parallelepiped, with some notable differences seen in Figure 1 below from [3].

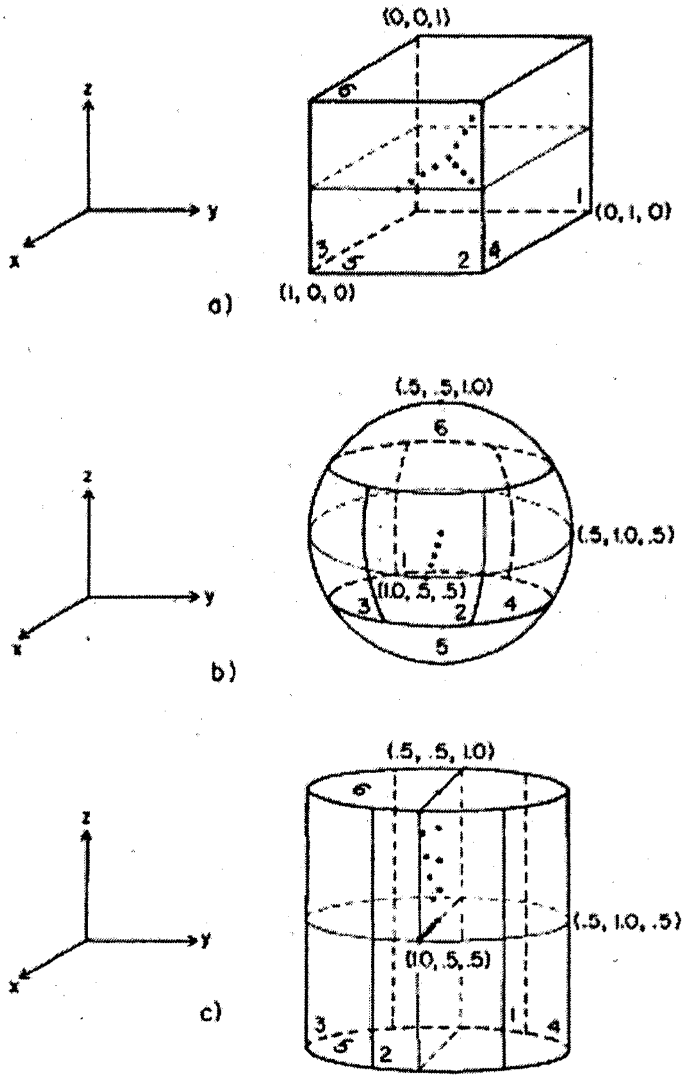

FIG. 1. Sketches of (a) the cubic, (b) the spherical and (c) the cylindrical cloud geometries used in this study. The numbers label the cloud faces, and the solid dots show the point-source locations computed for that geometry.

Since lightning primarily occurs in cumulonimbus clouds, it makes sense to investigate the results of a cylindrical shape as it is most similar in shape to a thunderstorm cloud [4].

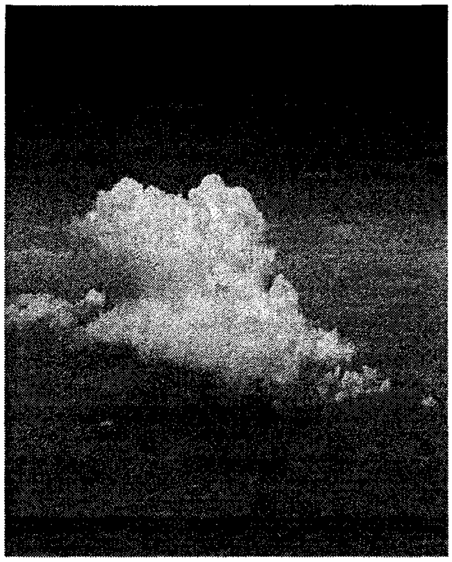

Figure 2: An example of a near cylindrically shaped cloud

The physical properties of a cloud and the patterns in the processes that it undergoes can be evaluated and analyzed mathematically for useful data such as forewarning, flash rate, rate of precipitation, intensity of radiation, rise times, time delays and analyses of past results. Satellites have been deployed in space to capture useful data. For example, all weather cloud formations and activity are monitored by various instruments, such as the Lightning Imaging Sensor (LIS) and Optical Transient Device (OTD) (Ch. 2).

Chapter 3 of this thesis provides a summary of reference [1], "Diffusion Model for Lightning Radiative Transfer" published by Koshak, Solakiewicz, Phanord, and Blakeslee. Reference [1] develops a model for studying lightning intensity inside a parallelepiped cloud. In Chapter 4, the research activity focuses on modeling lightning intensity inside a cylindrical cloud. Chapter 5 displays the results of the cylindrical model. Finally, comparison of the results of the cylindrical model to those of both the parallelepiped and spherical clouds are presented in Chapter 6.

1.1 Historical background of lightning

Lightning is a widely accepted indicator of bad weather and is both feared and respected for its possible destructive power, even back in ancient times. Before scientific studies of lightning were conducted, people struggled with explanations to natural phenomena such as lightning and thunder [4]. In Greek mythology, lightning was perceived as weapons of the gods, primarily used by Zeus. In Viking lore, the rumbling of thunder was attributed to the Norse god Thor riding his chariot across the clouds, with the clap of thunder representing his hammer striking an anvil while riding. In the East, early statues of Buddha had him holding thunderbolts with arrows at the end. The Egyptian god Typhon hurled thunderbolts when he was displeased with a matter. North American Indians explained the clapping of thunder as a mystical bird flapping it wings together, with the light in the clouds coming from the thunderbird's flashing wings. Even our own United States of America dollar bill has an eagle holding an olive branch in one claw and a thunder bolt in another, indicating both peace and strength, respectively.

Benjamin Franklin is noted as one of the first to conduct scientific experiments on lightning in the 18th century. Franklin theorized that clouds were electrically charged and inferred that a thunderbolt's charge from the cloud to the ground was negative. Some authors record his experiments with an iron rod and an isolated wax candle. Others record his experiments with a damped silk string attached to a kite held in one hand, and towards the end, a key from which sparks would fly to the other hand. Both experiments were conducted during thunderstorms [4]. Basically, Franklin as the grounded element completed a direct current circuit produced between the electrically charged cloud down the string to the key which created the sparks. Similar experiments were done in 1752 by

Thomas-Francois D'Alibard of France and in 1753 by G.W. Richmann of Sweden, who was working in Russia at the time. Richmann was killed during a lightning rod experiment, which attests to the dangers of lightning [4]. In the late 19th century, photography and spectroscopic tools were incorporated into lightning research. Notably, Pockels from Germany studied the magnetic fields formed by lightning. Into the 20th century, CTR Wilson won the Nobel Prize for inventing the Cloud Chamber (1927) [5], which he used in experimenting with supersaturated air in a container, passing electrons and alpha particles through it to discover their paths. His work motivated many other studies, including those involving x-rays, gamma ray collisions, ionizing particles and radiation. In 1932, BFJ Schonfield dedicated his book, Atmospheric Electricity, to CTR Wilson in appreciation and inspiration to continue his work [6].

1.2 What is lightning?

According to Uman [4], "lightning is a transient, high current electric discharge whose path lengths are measured in kilometers". In this definition, 'transient' means that lightning transfers energy from one place to another within a short period of time. High current electrical charge peaks at approximately 100 Kiloamps, but is normally about 40 Kiloamps with peak channel temperatures up to 30,000 Kelvin. The temperature of boiling water is 100^o Celsius or 212^o Fahrenheit or 373^o Kelvin. To estimate the temperature of the lightning channel, multiply the boiling temperature in Kelvin by a factor of 80 [4].

The most common means of categorizing lightning is by its path; i.e. (1) Intracloud lightning, (2) Cloud to Cloud lightning and 3) Cloud to ground lightning. The latter makes up 90% of worldwide lightning and is the target of most research as it can do the most damage. Berger (1975) [7] and Berger (1978) [8] categorize cloud to ground lightning further in terms of its direction of motion, upward or downward, and the sign of its charge, positive or negative. Cloud to ground strikes are either downward negatively charged leaders or downward positively charged leaders. Ground to cloud lightning strikes, usually coming from tall buildings or mountain tops, are upward moving positively charged leaders or upward moving negatively charged leaders. To clarify the differences in lightning types, specific names have been given to the different stages of lightning.

It is widely accepted that, within a cloud, a distribution of positive and negative charges exists [9]. However, when air is circulated in such a way that water droplets and/or ice crystals have an outer layer of positive charges stripped off, the remaining negative charges are separated. The cloud is then separated into positive charges at the top and negative charges at the bottom. The Earth is generally negative in clear weather. When a negative bottom cloud is formed above the Earth, positive charges from the Earth underneath the cloud are attracted to the surface of the Earth. Normally, the air acts as an insulator between the cloud and the Earth, but the negative charges of the cloud can become so strong that they are released. The cloud's negative charges are racing toward the Earth and the positive charges from the Earth are moving toward the cloud. They meet in an area closer to the Earth. Once connected, the channel through which the lightning will start its dart leader (to be defined below) is established [9].

Lightning is initiated within a cloud between the fields of positive and negative charges. This stage is called the preliminary breakdown. Less than one millisecond later, a discharge is sent both horizontally and downward in branches, which is termed the stepped leader. It denotes the start of motion towards the ground, bringing negative charges with it.

The situation described above is called the attachment process and occurs approximately in the tens of meters above the Earth's surface. The attachment process also involves the striking distance (SD), which is usually double the distance between the object on the Earth (to be) struck and where the attachment occurs. This phenomenon is carefully considered by architects and engineers in regards to lightning safety during the building design process [9].

The channel that is formed now has the ability to move positive charges from the Earth upward towards the cloud, and is called the return stroke. The return stroke is usually around 40 kiloamps in strength and acts as a neutralizer in the channel.

The dart leader is a new leader that occurs anywhere from 40-80 milliseconds later forming new branches from the original channel and as well as different paths to the ground, each with its own return stroke. This process continues to happen several times until the entire volume of the cloud is affected. For more details, see [9].

1.3 Importance of lightning – economic and global impact

The chance of being struck by lightning in the U.S. per year is approximately 0.00004% [10], a percentage so small that many think lightning could not affect them directly. However, the economic global impact of lightning is great. According to Krider [9], Physics of Lightning, the continental US receives approximately 40 million cloud to ground strikes annually (1978). According to NASA/Marshall Space Center statistics, approximately 100 people die in the US alone from lightning strikes annually, not including injuries and millions of dollars of property damage. Causes of death include heart damage, inflated lungs, electrical burns and/or brain damage. Survivors of lightning strikes experience loss of consciousness, amnesia, paralysis and extensive burns [10].

Due to the electromagnetic properties of lightning, strikes to electrical systems such as telecommunication systems, military systems, aircraft and spacecraft systems are capable of producing great damage. For example, the 1969 Apollo 12 lightning strike disabled an important part of the spacecraft's electrical system. The astronauts were able to regain control in that incident, but for the Atlas Centaur 670 in 1987, a lightning strike caused the craft to break up. The possibility of lightning occurrence is taken very seriously when planning an appropriate day and time of lift-off for these multibillion dollar space vehicles. Even smaller commercial airlines fear for both the safety of their passengers and possible damage to their aircraft by lightning strikes, which causes delays in flight time for both inbound and outbound flights when clouds are looming near an airport. The effects of lightning are indeed ubiquitous!

Some forest fires are started by lightning strikes, which result in loss of habitat, and often, economic setbacks. Many animals lose their homes and trees are lost. Along with the advancement of society and the need to build more homes, more forestry is being lost by greed than lightning.

There are positive effects of lightning in nature. For example, lightning is a natural fertilizer and non-equalizer of trace gases in the atmosphere. Lightning helps maintain the balance of electrical charges on Earth and is an important phenomenon in the study of electromagnetic wave propagation and its geophysical aspects.

CHAPTER 2

PHYSICAL PHENOMENON OF LIGHTNING

The physics involved between lightning and the atmosphere must be considered in order to develop an appropriate model for lightning intensity. The Lorentz gas model is used in this thesis due to the fact that all scatterers present in the model must have the location of their centers fixed. In addition, the Lorentz gas model considered here is assumed to be composed of identical spherical water droplets. Furthermore, the photons generated by lightning events are permitted to make only elastic collisions.

The layers of the atmosphere are important to study as lightning only occurs under certain conditions and therefore occurs only in certain parts of the atmosphere [4]. It is crucial to know under what conditions lightning is generated. One of the factors in lightning production is that the ambient temperature must be between -10 and -20 degrees Celsius [9]. This fact suggests where lightning is most likely to occur [3]. Thus, there must be an analysis of how each layer of the atmosphere differs from the others, along with the chemical constituents of each layer. There must also be a threshold level of moisture content to produce the visible cloud. Therefore, the relationship between lightning and the rate of precipitation must be considered. It has been recently reported that ice formations relative to the rate of lightning strikes can lead to more severe weather conditions such as hurricanes [15]. Lightning affects the ozone layer, which protects the Earth from harmful rays of the sun. The practical importance of the study of lightning is so great that our nation and other countries have launched lightning detection instruments into space, along with other weather detection devices, to study and analyze patterns of occurrences of destructive storms.

2.1 Layers of the atmosphere

There are basically five layers of the atmosphere: the troposphere, stratosphere, mesosphere, thermosphere and exosphere. There are also thin layers that separate the above five layers, such as the tropopause, stratopause, mesopause, thermopause and an important layer called the ionosphere. The National Oceanic & Atmospheric Administration (NOAA) describes the layers according to temperature ranges, chemical composition, movement and density [11].

The troposphere is the layer closest to the Earth, where most of the weather occurs due to the instability of the air. This layer extends from the Earth's surface up to 4-12 miles (6-20km) in elevation [11]. As altitude increases, temperature decreases and the air becomes thinner. The temperature in this layer ranges from 17 to -52 degrees Celsius [11]. Because of the instability of the air, clouds are formed, particularly cumulonimbus clouds. As charges within the cloud separate, lightning is produced within and outside of the cloud and thunder is heard; hence, the term thunderstorms. Aircraft often experience turbulence in the troposphere, and since the cumulonimbus clouds which produce thunderstorms can reach heights of 39,000 feet, aircraft generally fly around 35,000 feet or anywhere above the clouds. Some jet aircraft even go as far the lower stratosphere to attain stable air.

The stratosphere ranges from the tropopause up to 31 miles (49.9 km) in altitude. This layer has very little water vapor, and as altitude increases, temperature increases. The temperature in this layer increases to -3 degrees Celsius [11]. The stratosphere also contains the ozone layer, which helps protect us from the harmful ultraviolet rays of the sun. The breakdown of the ozone layer is of much concern because of its contribution to global warming. Lightning plays a factor in producing nitrogen oxides (NO_x) which can be harmful at lower levels of the atmosphere but beneficial in the stratosphere for increasing the level of the ozone layer [12], [13]. The main producer and harmful contributor to the depletion of the ozone layer is the burning of fossil fuels. NASA, among others, is studying the effect of lightning and burning of fossil fuels on the atmosphere using satellite instruments.

The mesosphere extends from the stratopause up to 53 miles (85 km) in elevation. In this layer, as altitude increases, temperature decreases. The slow movement of gases in this layer slows down the movement of incoming meteors, causing nearly all of them to burn up prior to reaching the Earth. The cold temperatures at this level, as low as -93^o Celsius [11], also help protect us from the intense incoming heat from the sun.

The thermosphere spans from the mesosphere 53 miles up to 430 miles (690 km). This is the layer of the atmosphere where the space shuttle and satellites orbit. The air in this layer is a million times thinner than air at the Earth's surface. The temperature at this level is 3600^o Fahrenheit or 2000^o Celsius. Even with this high temperature, the air would still feel cold because of how thin it is and the few molecules that are present are far apart. The ionosphere is embedded within the thermosphere, which is important because of its ability to bounce transmitted radio signals back to the Earth, such as satellite TV, radio and GPS systems.

The exosphere extends from the thermopause up to 6200 miles (10,000 km) and is the thin layer prior to outer space. The temperature may reach as high as 1727^o Celsius [11]. This is the layer in which atmospheric conductivity is greatest and where gases and molecules can escape from the atmosphere.

Uman [4] (1987, pg 30) describes the thunderstorm as a battery, in that it keeps the Earth negatively charged and the atmosphere positively charged. This is important in the modeling of lightning intensity, since a key assumption is that no energy is lost, or photons allowed to escape - hence, no back-scattering. Understanding what occurs at different layers of the atmosphere is important because it provides clues as to how to help best protect our resources on Earth.

2.2 Lightning and the ozone

The chemical structure of each of the layers of the atmosphere is important to understand because chemicals that affect ozone react differently to lightning in one layer versus another. Atmospheric chemistry is associated with the chemical reactions that occur in the atmosphere from natural and man-made chemicals. Lightning strikes produce intense heat and electrical current that break up the main molecular components of the troposphere, namely Nitrogen (N_2) and Oxygen (O_2). These can be recombined/reformulated into nitrous oxide compounds such as NO, NO_2, and NO_x, the latter of which affects the ozone layer. Ozone is produced by the binding of three oxygen atoms into an O_3 molecule, which can affect changes in climate because of its greenhouse effect [12], [13].

Zhang [12] stated that lightning is responsible for 90% NO in summer, with a corresponding 30% increase in ozone levels in the troposphere (3-8 miles above the Earth's surface). Zhang states that there are 77 million lightning bolts per year in the U.S. and 60 lightning flashes per second worldwide. He further states that urban air pollution and warming of the Earth can produce more lightning.

In an August 2007 study commissioned by NASA and the U.S. Office of Naval Research [14], a climate model simulated the strength of winds and updrafts in storms both on land and in the ocean. The model, developed at NASA's Goddard Institute for Space Studies, theorizes that the warming of the Earth will cause more severe storms but fewer storms overall. Although the model does not simulate lightning and thunder directly, it does suggest the conditions under which storms are likely to occur. The model's simulated data is consistent with the instrument data, in that there is more lightning in the tropical continents, such as Africa, and very little lightning over the ocean.

In the model, the carbon dioxide level and the temperature of the Earth's surface can be changed. In a specific example given in the study, the carbon dioxide level was doubled and the Earth warmed in that area by 5^{o} Fahrenheit. The model reported strong updrafts along with horizontal winds, causing lightning to occur at higher altitudes, which resulted in more severe storms.

A subsequent 2007 NASA study [15] focused on the connection between lightning occurrences in the eyewall of a hurricane and possible correlations with its strength.

> "Hurricane's eyewall is the inner heat driven region of the storm that surrounds the 'eye' where the most intense rainfall and most powerful winds occur by monitoring the intensity of lightning near a hurricane's eye, scientist will be able to improve forecasts of when a storm may unleash its harshest conditions."

To test this theory, a combination of lightning data sets from several detection instruments were analyzed, such as ground based networks (PLDN), space based instruments (LIS and Microwave Imager) and aircraft based sensors ('hurricane hunter') that actually fly through a storm to collect data. This article uses data from both the TRMM's Microwave Imager and Lightning Imaging Sensor (LIS). The Microwave Imager measures the temperature and concentration of ice particles, while the LIS measures lightning occurrences within the eyewall. This study used data from the Category 5 hurricanes Katrina and Rita in 2005.

Ice formation in the eyewall was also considered. "Ice is important for charge separation and is needed to produce lightning." [15]. The process starts when water condenses from vapor to droplets and latent heat is released, causing updrafts. If the updrafts are strong enough, they cause a separation of charge which produces lightning, thereby releasing more energy, which in turn fuels the hurricane [15].

In [15], it is stated that there are intercorrelations among (a) the rate of lightning strikes; (b) the amount of rainfall; and (c) the heat released in the eyewall of a storm.

By examining these factors together, the study claims that the computer model can forecast the hurricane's track and intensity. By the end of 2008, the PLDN will include eight more ground based lightning detection sensors that can detect lightning events occurring thousands of miles away. Research efforts continue in this field to try to predict the strength of an upcoming hurricane which, if properly considered by government officials to forewarn citizens, can result in saving lives.

2.3 Connection of lightning and precipitation

The correlation between lightning and precipitation can be readily studied from the components of the TRMM satellite. The five major components of the TRMM are the LIS (Lightning Imaging Sensor), the PR (Precipitation Radar), the VIRS (Visible Infrared Scanner), the CERES (Cloud and Earth Radiant Energy System) and the TMI (TRMM Microwave Imager). These components allow scientists to gain a global view of weather patterns, thereby providing them with means to investigate interrelationships among lightning, precipitation, and latent heat. As implied by the name Tropical Rainfall Measurement Mission, TRMM monitors convective storms in the tropics, a lightning rich environment.

Lightning primarily occurs in cumulonimbus clouds because of turbulent air. There must be high moisture content in the cloud. Cooler air exists at the top of the cloud because within the troposphere, where most weather occurs, the higher the altitude, the cooler the temperature. Air has upward drafts that strip off the negative charges of water droplets and ice crystals, and carries the positive charges to the top of the cloud. Conversely, downward drafts transport the negative charges to the bottom of the cloud.

Once the air cools, the moisture in the cloud droplets becomes heavy enough that they fall out of the clouds in the form of precipitation. Once the precipitation is released, the negatively charged cloud bottom will try to connect to the Earth's surface, which is positively charged under a thundercloud. As Christian explains in reference [16], lightning follows the same path, which allows identification of the common regions of lightning occurrence and also indicates the amount of rainfall. This has been shown to be directly related to the lightning flash rate.

2.4 Lightning detection instruments

Lightning detection instruments have gone through many improvements over time, such as range capabilities and increases in accuracy of measurements. These instruments evolved from ground based instruments to space based instruments. Starting out as a field model, the National Lightning Detection Network (NLDN) was used to detect cloud to ground lightning strikes from 100 kilometers away, but it did not have the capacity to detect intra-cloud lightning. The Lightning Detection and Ranging (LDAR) sensors are located near the Kennedy Space Center and can detect 99% of lightning occurrences via both intra-cloud and cloud-to-ground means, but it only has a range of 10 kilometers. Scientists went to the air and used several lightning detection instruments attached to jet aircraft to see if they could detect changes in the electrical charges of the atmosphere during a storm. Scientists then went up higher, launching a space based instrument in April 1995 called the Optical Transient Device (OTD) on the Microlab 1 satellite, later renamed the OV-1 satellite. Also, the Lightning Imaging Sensor (LIS) was launched as part of the Tropical Rainfall Measuring Mission (TRMM) sponsored by

NASA and the Japanese Space Program. These space-based instruments are extremely useful because they provide a global view of lightning occurrence, not simply for one region or one continent.

2.4.1 Optical Transient Detector (OTD)

Scientists from the Orbital Science Corporation only had nine months from design, fabrication, and calibration to deliver OTD onboard the Pegasus satellite in May 1995. However, OTD far exceeded expectations for its use. Its mission was intended to last for two years. However, with a detection efficiency of 40-65% in both daytime and nighttime lightning occurrences around the world, its mission ultimately lasted for 5 years. OTD orbited the Earth at a 70^o inclination relative to the equator at an altitude of 240 km. Its 100^ox 100^o field of view covered a 1300 x 1300 km region, which according to the authors of [17], is 1/300 of the total surface area of the Earth.

The authors of [17] describe the OTD as a solid state optical sensor similar to a television camera which has a detector array similar to the human eye with circuitry to convert electrical output into useful data. Since the OTD is very similar to a television camera, lightning detection is done on a frame by frame comparison. The difference between frames is assigned a threshold energy level which, if exceeded, is recorded as an "event". If more than one event is recorded in a 2 microsecond timeframe, it is called a "group", and if more than one group is recorded, a lightning "flash" is said to occur.

2.4.2 Lightning Imaging Sensor (LIS)

The Lightning Imaging Sensor (LIS) head, of dimension 20x37 cm, is housed in a 31x22x27 cm. telescope weighing only 20 kg. (approximately 44 lbs.) As Christian, et al. describe in [16], the LIS is a small, solid state optical imager that detects lightning from low Earth orbit with high detection efficiency and location accuracy. It marks the time of occurrence of lightning flashes, and measures their radiant energy. The major elements of the LIS are the imaging system, the focal plane assembly, the real-time signal processor, the background remover, the event processor and formatter, the power supply and the interface electronics [16].

The LIS orbits the Earth at 350 km. altitude at a 35 degree inclination relative to the equator with a velocity of 7 km/s. The 80^o x 80^o field of view covers an area of 580 by 580 km. Although there is a decrease in the field of view relative to the OTD, there is an increase in detection efficiency of lightning from 40-65% (OTD) to 90% (LIS), due to many improvements such as the sampling rate, which is greater than 500 frames per second, resulting in a 2 ms time resolution.

CHAPTER 3

SUMMARY OF DIFFUSION MODEL FOR LIGHTNING RADIATIVE TRANSFER

In reference [1], a diffusion model for lightning radiative transfer was presented. The work done in [1] started with a simplified version of the generalized Boltzmann transport equation from kinetic theory which is consistent with the Lorentz gas model.

3.1 The Boltzmann Transport Equation

Starting with equation (1) of reference [1], we have

$$\frac{\partial I(\vec{r},\hat{\Omega},t)}{\partial t} = -c\hat{\Omega}\cdot\nabla I(\vec{r},\hat{\Omega},t) + c\omega_0 K(\vec{r})\int_{4\pi} p(\hat{\Omega}\cdot\hat{\Omega}')I(\vec{r},\hat{\Omega}',t)d\hat{\Omega}' - cK(\vec{r})I(\vec{r},\hat{\Omega},t) + \frac{\partial Q(\vec{r},\hat{\Omega},t)}{\partial t}, \qquad (1)$$

where $I(\vec{r},\hat{\Omega},t)$ is the particle intensity, c is the speed of light, $\hat{\Omega}$ is the direction of the particle given an arbitrary direction of incidence $\hat{\Omega}'$, ω_0 is a single scattering albedo which defines the probability that a collision will result in a scattering event, $K(\vec{r})$ is the inverse mean free path, $\int_{4\pi}$ denotes integration over the whole volume, $p(\hat{\Omega}\cdot\hat{\Omega}')$ is the probability that a particle will scatter, and $Q(\vec{r},\hat{\Omega},t)$ is the source intensity. The model described by equation (1) is represented by Figure 3. This particular model is selected because the scattering centers are not allowed to recoil, so no energy is exchanged

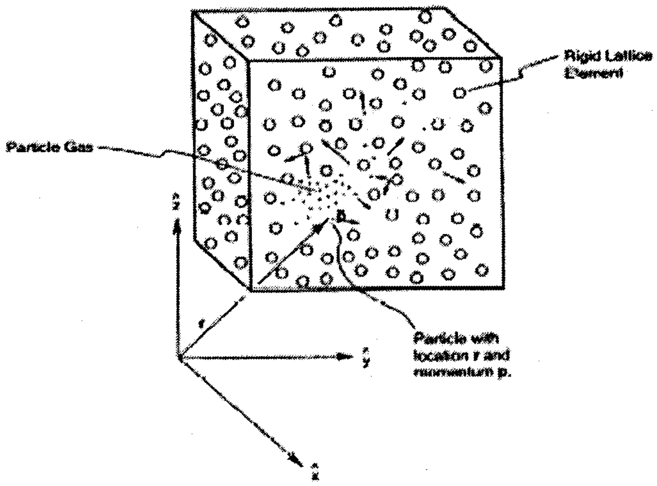

Figure 3: Illustration of the Lorentz gas model for particle transport. A gas of noninteracting particles randomly walk as they make elastic collisions with a rigid scattering lattice. Particle positions and momentum are denoted by $\vec{r}$ and $\vec{p}$, respectively.

in collision events. Therefore, the use of a one-speed Boltzmann transport equation is appropriate. By contrast, random walk or self-diffusion processes apply when particles of interest diffuse through a background medium, interacting randomly via collisions with the microscopic structure of the medium. Related to this is the concept of a collective phenomenon, in which particles of interest diffuse and interact among themselves. Its mathematical description would require a nonlinear transport equation which is beyond the scope of this research. A Lorentz gas model has a random array of fixed scattering centers. In this study, the lightning photons produced are the particles that are randomly walking through a medium, which is a rigid collection of identical spherical water droplets.

3.2 Diffusion approximations

Equation (1) is solved with a diffusion approximation, since the Boltzmann transport equation has no known analytic solution. Consequently, we expand the terms I, Q and p of equation (1) using spherical harmonics (Y_{lm}) equations developed in Arfken (1968) [18]:

$$I(\vec{r},\hat{\Omega},t)=\sum_{L=0}^{\infty}\sum_{M=-L}^{L} I_{LM}(\vec{r},t)Y_{LM}(\hat{\Omega}),$$

$$Q(\vec{r},\hat{\Omega},t)=\sum_{L=0}^{\infty}\sum_{M=-L}^{L} Q_{LM}(\vec{r},t)Y_{LM}(\hat{\Omega}), \tag{2}$$

$$p(\hat{\Omega}\cdot\hat{\Omega}')=\frac{1}{\omega_0}\sum_{L=0}^{\infty}\sum_{M=-L}^{L}\frac{\omega_L}{2L+1}Y^{*}{}_{LM}(\hat{\Omega}')Y_{LM}(\hat{\Omega}).$$

Working with equation (2), equation (1) and the orthogonality principle given by [1], the authors of [1] deduced that

$$\frac{\partial I_{LM}}{\partial T}=-c(A_{LM}(\vec{r},t)[1-\frac{\omega_L}{2L+1}]I_{LM}(\vec{r},t))+\frac{\partial Q_{LM}(\vec{r},t)}{\partial t},$$

where $A_{LM}(\vec{r},t)=\int_{4\pi}\sum_{L'=0}^{\infty}\sum_{M'=-L'}^{L'}\hat{\Omega}\cdot\nabla I_{L'M'}(\vec{r},t)Y_{L'M'}(\hat{\Omega})d\hat{\Omega}$. (3)

Equation (3) represents an infinite collection of coupled differential equations. Using Williams' (1971) [19] method of truncation at L=1 and setting $I_{LM}=0$ whenever $L\geq 2$, equation (3) is recast into a set of two equations given by

$$\frac{\partial\rho}{\partial t}+\nabla\cdot\vec{J}+(1-\omega_0)Kc\rho-\frac{\partial\rho_Q}{\partial t}=0$$

and

$$\frac{\partial\vec{J}}{\partial t}+\frac{c^2}{3}\nabla\rho+(1-g\omega_0)Kc\vec{J}-\frac{\partial\vec{J}_Q}{\partial t}=0. \tag{4}$$

Hence, the diffusion variables ρ and J are given by

$$\rho(\vec{r},t) \equiv \int_{4\pi} I(\vec{r},\hat{\Omega},t)d\hat{\Omega} = \sqrt{4\pi}I_{00}$$

and

$$\vec{J}(\vec{r},t) \equiv \int_{4\pi} I(\vec{r},\hat{\Omega},t)c\hat{\Omega}d\hat{\Omega} = c\sqrt{\frac{2\pi}{3}}\begin{bmatrix} I_{11}-I_{1,-1} \\ i(I_{11}+I_{1,-1}) \\ \sqrt{2}I_{10} \end{bmatrix}. \qquad (5)$$

The new quantities ρ_Q and $\vec{J}_Q$ are source terms similar to ρ and $\vec{J}$ of the above equations where $I(\vec{r},\hat{\Omega},t)$ is replaced by $Q(\vec{r},\hat{\Omega},t)$. In addition, the asymmetry factor g is defined

as $$g \equiv \frac{\int_{-1}^{1}(\hat{\Omega}\cdot\hat{\Omega}')p(\hat{\Omega}\cdot\hat{\Omega}')d(\hat{\Omega}\cdot\hat{\Omega}')}{\int_{-1}^{1}p(\hat{\Omega}\cdot\hat{\Omega}')d(\hat{\Omega}\cdot\hat{\Omega}')}. \qquad (6)$$

The value of g in reference [1] is the forward peaked anistropic scattering at g=0.84, which is consistent with backward scattering at g=-1, anistropic scattering at g=0 and complete forward scattering at g=1. Moreover, $\omega_0 = 0.99996$ describes the case of near conservative scattering. The intensity distribution using the truncation at L=1, $I_{LM} = 0(L \geq 2)$ was given in [1] by

$$I(\vec{r},\hat{\Omega},t) \approx I_{00}Y_{00} + I_{1,-1}Y_{1,-1} + I_{10}Y_{10} + I_{11}Y_{11} = \frac{1}{4\pi}[\rho + \frac{3}{c}\vec{J}\cdot\hat{\Omega}]. \qquad (7)$$

Eliminating the first and fourth terms in equation (7), the authors of [1] obtained

$$\frac{\partial\rho}{\partial t} = -\nabla\cdot\vec{J} - (1-\omega_0)K(\vec{r})c\rho + \frac{\partial\rho_Q}{\partial t},$$

$$\vec{J} = -\frac{c}{3K(\vec{r})(1-g\omega_0)}\nabla\rho \equiv -D(\vec{r})\nabla\rho, \qquad (8)$$

which are the standard diffusion equations with diffusion coefficient

$$D(\vec{r}) = \frac{c}{3K(\vec{r})(1-g\omega_0)}.$$

3.3 Boundary conditions

To solve the proposed equation (3), the authors of [1] had to solve equation (8) for ρ and $\vec{J}$ with imposed initial and boundary conditions. Allowing time equal to zero (t=0) to represent a time just prior to any lightning occurrence event and assuming that there is no backscattering, then

$$I(\vec{r}_s,\hat{\Omega},t) = 0, \qquad (\vec{n}\cdot\hat{\Omega}) < 0. \tag{9}$$

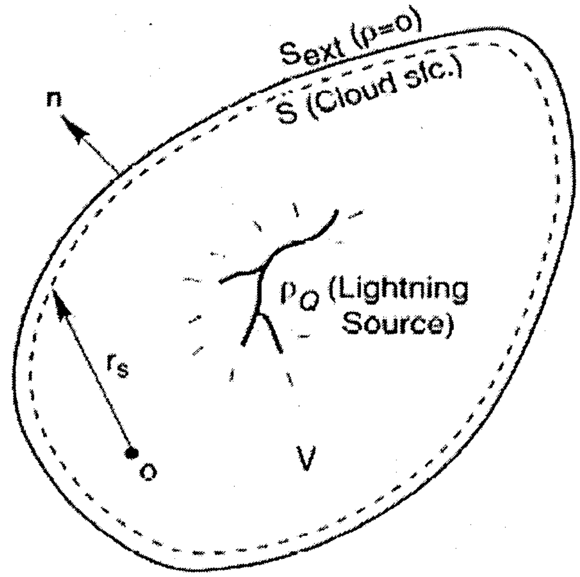

Figure 4: The solution space V for the intensity solution $I(\vec{r},\hat{\Omega},t)$. *The convex extrapolation surface* S_{ext} *bounds V, and has unit normal* $\vec{n}$. *The surface S defines the true cloud surface and isotropic lightning source function,* $\rho_Q(\vec{r},t)$ *is shown. The origin of the coordinate system, O, and positions on S are also indicated.*

where $\vec{r}_s$ is a point on the cloud's surface. To keep photons from scattering back into V, a leaky boundary condition given by Duderstadt and Martin (1979) [20] is used:

$$\vec{n}\cdot\int_{2\pi} I(\vec{r}_s,\hat{\Omega},t)c\hat{\Omega}d\hat{\Omega}=0, \qquad (\vec{n}\cdot\hat{\Omega})<0. \tag{10}$$

3.4 Sturm-Liouville solution

The Sturm-Liouville problem with initial and boundary conditions used in [1] is the following:

$$\begin{aligned}
&\frac{\partial\rho(\vec{r},t)}{\partial t}+\mathcal{L}\rho(\vec{r},t)=\frac{\partial\rho_Q(\vec{r},t)}{\partial t}, && \vec{r}\in V; \\
&\rho(\vec{r},t)=0, && \vec{r}\in S_{ext}; \\
&\rho(\vec{r},0)=0, && \vec{r}\in V,
\end{aligned} \tag{14}$$

where $\mathcal{L}=-\nabla\cdot[D(\vec{r})\nabla]+(1-\omega_0)K(\vec{r})c$ is the linear self-adjoint operator which has complete orthogonal eigenfunctions and whose solution is of the form

$$\rho(\vec{r},t)=\sum_{i=1}^{\infty}\alpha_i(t)\Psi_i(\vec{r}), \qquad \vec{r}\in V. \tag{15}$$

To obtain the eigenfunctions and eigenvalues, the authors of [1] used

$$\begin{aligned}
&\lambda_i^2\Psi_i(\vec{r})=\mathcal{L}\Psi_i(\vec{r}), && \vec{r}\in V; \\
&\Psi_i(\vec{r})=0, && \vec{r}\in S_{ext},
\end{aligned} \tag{16}$$

which leads us to the ordinary differential equation

$$\begin{aligned}
&\frac{d\rho_i(t)}{dt}+\lambda_i^2\rho_i(t)=\frac{d\rho_{Q_i}(t)}{dt}, \\
&\rho_i(0)=\int_V \Psi_i(\vec{r})\rho(\vec{r},0)dV,
\end{aligned} \tag{17}$$

where $\rho_i(t) \equiv \int_V \Psi_i(\vec{r})\rho(\vec{r},t)dV$ is an eigentransformed diffusion variable.

The solution of equation (17) is

$$\rho(\vec{r},t) = \sum_{i=1}^{\infty} \frac{\Psi_i(\vec{r})}{\int_V \Psi_i^2(\vec{r})dV} e^{-\lambda_i^2 t}(\rho_i(0) + \int_0^t e^{\lambda_i^2 t'} \frac{\partial \rho_{Q_i}(t')}{\partial t'} dt'). \tag{18}$$

Working with equations (7) and (8), together with equation (18), the intensity distribution inside V can be calculated. For a homogeneous parallelepiped cloud, N transient point sources are used and allowed to be turned on and off simultaneously or in arbitrary succession. The source derivative may be written as

$$\frac{\partial \rho_Q(\vec{r},t')}{\partial t'} = \sum_{j=1}^{N} w_j \delta(\vec{r} - \vec{r}_j)\delta(t' - t_j), \tag{19}$$

where w_j, the weighting factor, represents the photon strength at location $\vec{r}_j$ at time t_j. Solving the Sturm-Liouville problem for the eigenfunctions $\Psi_{lmn}(\vec{r})$ and the corresponding eigenvalues λ_{lmn}^2, we obtain

$$\Psi_{lmn}(\vec{r}) = \sin(\frac{\pi l x}{d_x})\sin(\frac{\pi m y}{d_y})\sin(\frac{\pi n z}{d_z})$$

and

$$\lambda_{lmn}^2 = D\pi^2[(\frac{l}{d_x})^2 + (\frac{m}{d_y})^2 + (\frac{n}{d_z})^2] + (1 - \omega_0)Kc. \tag{20}$$

The subscript (l,m,n) is representative of the parallelepiped, and thus for a cylindrical cloud, would be (ρ, θ, z) instead of the subscript i. Using the solution $\rho(\vec{r},t)$ of equation (18), the standard diffusion equations (8), and the truncation scheme of equation (7), we obtain the intensity distribution inside V for a parallelepiped cloud:

$$I(\vec{r},\hat{\Omega},t)=\frac{2}{\pi V}\sum_{l=1}^{\infty}\sum_{m=1}^{\infty}\sum_{n=1}^{\infty}[\Psi_{lmn}(\vec{r})-\frac{3D}{c}\hat{\Omega}\cdot\nabla\Psi_{lmn}(\vec{r})]\sum_{j=1}^{N}\omega_j\Psi_{lmn}(\vec{r}_j)e^{-\lambda_{lmn}^2(t-t_j)} \quad (21).$$

Equation (21) represents the final mathematical physics solution of the problem at hand. The model presented here will be used to treat the case of a cylindrical cloud.

CHAPTER 4

ANALOGUE IN CYLINDRICAL COORDINATES

This chapter deals with the cylindrical model for lightning radiative transfer using the theory published in reference [1] and summarized in Chapter 3 of this thesis. This research works with a circular cylinder of radius $\rho = a$ and height z=L. The origin of coordinates is located at the center of the circular base of the cylinder, while the z-axis is its axis of symmetry. For more details, see Figure 5 below.

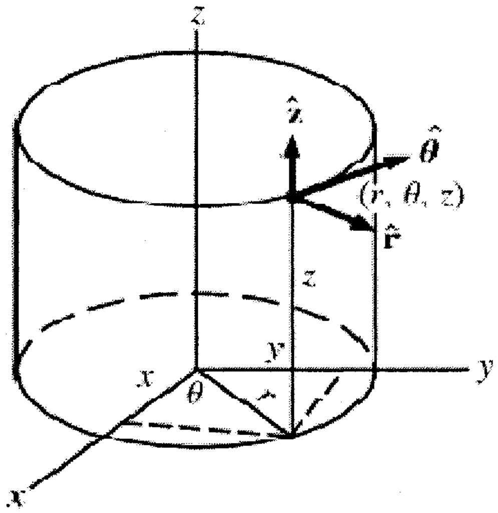

Figure 5: An example of a circular base cylinder with z-axis as its axis of symmetry.

4.1 Sturm-Liouville problem

The main objective of this chapter is to derive the analogue of equation (21) of reference [1]. This is accomplished by solving equation (16) of reference [1] or equation (16) of Chapter 3 in cylindrical coordinates:

$$\lambda_i^2\Psi_i(\vec{r}) = \mathcal{L}\Psi_i(\vec{r}), \qquad \vec{r} \in V;$$

$$\lambda_i^2(\vec{r}) = 0, \qquad \vec{r} \in S_{ext}, \tag{22}$$

where V is the volume of the cylinder and S_{ext} is its exterior surface as presented in both reference [1] and Chapter 3 of this work. The operator $\mathcal{L}$ is defined as $\mathcal{L} = -\nabla\cdot[D(\vec{r})\cdot\nabla] + (1-\omega_o)K(\vec{r})c$. The derivation will begin by working with the operator $\mathcal{L}$ and equation (22).

Substituting $\mathcal{L}$ in the first part of equation (22) and after simplification, we obtain, while holding $D(\vec{r})$ constant,

$$(\nabla^2 + k^2)\Psi_i(\vec{r}) = 0,$$

$$k^2 = [\lambda_i^2 - (1-\omega_o)K(\vec{r})c]/D(\vec{r}). \tag{23}$$

4.2 Separation of variables

To solve equation (23) in cylindrical coordinates, the method of separation of variables is used. The function $\Psi(\vec{r})$ is written as the product

$$\Psi = R(\rho)\Theta(\theta)Z(z). \tag{24}$$

Using (24), and substituting the cylindrical form of Laplace's operator

$$\vec{\nabla}^2 \equiv \frac{1}{\rho}\frac{\partial}{\partial\rho}(\rho\frac{\partial}{\partial\rho}) + \frac{1}{\rho^2}\frac{\partial^2}{\partial\theta^2} + \frac{\partial^2}{\partial z^2} \tag{25}$$

given by Arfken [21] into equation (23) leads to

$$\frac{1}{\rho}\frac{\partial}{\partial\rho}(\rho\frac{\partial R\Theta Z}{\partial\rho})+\frac{1}{\rho^2}\frac{\partial^2 R\Theta Z}{\partial\theta^2}+\frac{\partial^2 R\Theta Z}{\partial z^2}+k^2 R\Theta Z=0\,. \tag{26}$$

Applying the standard technique of separation of variables generates the following three ordinary differential equations:

$$\begin{aligned}&\text{(a)}\ \frac{d^2 Z}{dz^2}+\gamma^2 Z=0\,;\\ &\text{(b)}\ \frac{d^2\Theta}{d\theta^2}+m^2\Theta=0\,;\\ &\text{(c)}\ \rho^2\cdot\frac{d^2 R}{d\rho^2}+\rho\frac{dR}{d\rho}+(\alpha^2\rho^2-m^2)R=0\,,\end{aligned} \tag{27}$$

where $k^2-\gamma^2=\alpha^2$ and m and γ are constants whose values are to be determined based on the boundary conditions given in equation (22). For more details, see Appendix A.

Equation (27) is composed of three parts; solving for part (a) and part (b) with the boundary conditions of equation (22) gives

$$Z(z)=A_z\sin(\frac{m\pi}{L}z),\quad \Theta(\theta)=A_\theta\sin(n\theta)\,, \tag{28}$$

where $\gamma=\frac{m\pi}{L}$, with m and n denoting positive integers. The third part of equation (27) is more complicated; to deal with it, we make the change of variables $q=\alpha\rho$ to obtain

$$q^2\frac{d^2 R}{dq^2}+q\frac{dR}{dq}+(q^2-n^2)R=0\,. \tag{29}$$

Recognizing that equation (29) is a Bessel equation of order n, its solutions can be written

$$R(\rho)=A_\rho J_n(\alpha\rho)+B_\rho Y_n(\alpha\rho)\,, \tag{30}$$

which reduces to

$$R(\rho) = A_\rho J_n(\alpha\rho) \tag{31}$$

due to the singularity of $Y_n(\alpha\rho)$ at $\rho = 0$ and the fact that the solution of the problem must be continuous at $\rho = 0$. To completely determine $R(\rho)$, we must evaluate the constant α.

Using the condition that the solution must vanish at $\rho = a$ leads to

$$J_n(\alpha\rho)=0, \qquad \chi_{ln} = \alpha a, \qquad \alpha = \frac{\chi_{ln}}{a}. \tag{32}$$

Observe that equation (32) is a transcendental equation and the χ_{ln} are its l roots (l being an integer). Combining equations (28), (31), and (32) with the product definition of $\Psi_i(\vec{r})$, we obtain the formal functional form for the solutions of equations (22) in cylindrical coordinates as

$$\Psi_{lmn}(\rho,\theta,z) = J_n(\frac{\chi_{ln}}{a}\rho)\sin(n\theta)\sin(\frac{m\pi}{L}z). \tag{33}$$

Equation (33) is the cylindrical analogue of equation (20) of reference [1].

4.3 Cylindrical Analogue of Equation (21) of [1]

To obtain the cylindrical analogue of equation (21) of reference [1], the following steps have been implemented:

(a) The cylindrical functional form of Ψ_{lmn} of equation (33) is substituted into equation (18).

(b) The value of $\int_V \Psi^2_{lmn}(\vec{r})dV$ is obtained.

(c) The result of $\hat{\Omega}\cdot\vec{\nabla}\Psi_{lmn}$ is derived.

Using the above mentioned values and derivations, and working similarly to reference [1] with equations (7) and (8), the cylindrical analogue of equation (21) of reference [1] is given by

$$I(\vec{r},\hat{\Omega},t)=\frac{a^2}{2\pi V\int_0^a J_n^2(\frac{\chi_{nl}}{a}\rho)d\rho}\cdot\sum_{l=1}^{\infty}\sum_{m=1}^{\infty}\sum_{n=1}^{\infty}[J_n(\frac{\chi_{ln}}{a}\rho)\sin(m\theta)\sin(\frac{n\pi}{L}z)]-\frac{3D}{c}$$

$$\cdot[\frac{1}{2}[J_{n-1}(\frac{\chi_{ln}}{a}\rho)-J_{n+1}(\frac{\chi_{ln}}{a}\rho)]\sin\theta+[\frac{n\pi}{L}\cos(\frac{n\pi}{L}z)\cos\theta]$$

$$\cdot[\sum_{j=1}^{N}\omega_j\Psi_{lmn}(\vec{r}_j)e^{-\lambda_{lmn}^2(t-t_j)}]. \qquad (34)$$

The details of the calculations leading to equation (34) are provided in Appendix B.

CHAPTER 5

NUMERICAL CALCULATIONS, GRAPHICAL REPRESENTATION AND ANALYSIS

In this chapter, numerical results pertaining to lightning radiative transfer generated by the cylindrical cloud are presented. Graphs of the intensity of radiation versus time are provided for cases corresponding to different mean free paths, sizes, and angles. The numerical codes used in this thesis originated from the work done in [1]. They were modified to meet the constraints of the cylindrical geometry of this model. The necessary approximations and values required for the attached simulations and graphical representations are described below.

5.1 Information needed to simulate and graph the results of the model

Starting with equation (23) of Chapter 4, we have

$$[\nabla^2 + k^2]\Psi_i(\vec{r}) = 0\,,\ \vec{r} \in V\,, \qquad \iota = 1,2,3,....$$

$$\Psi(\vec{r}) = 0\,, \qquad \vec{r} \in S_{ext}\,.$$

Next, equation (33) of Chapter 4 is

$$\Psi(\vec{r}) = \Psi(\rho,\theta,z) = \sum_{l=1}^{\infty}\sum_{m=1}^{\infty}\sum_{n=1}^{\infty} J_n((\frac{\chi_{ln}}{a})\rho)\cdot \sin n\theta \cdot \sin(\frac{m\pi}{L})z\,.$$

Using the approximation function for J_n in reference [21], this becomes

$$\Psi(\vec{r}) = [\sqrt{\frac{2}{\pi(\frac{\chi_{ln}}{a}\rho)}} \cdot \cos(\frac{\chi_{ln}}{a}\rho - \frac{3\pi}{4})]\sin(n\theta)\sin(\frac{m\pi}{L}z)\,. \tag{35}$$

Working with $n = m = 1$ and the variables listed below:

$\chi_{ln} = \chi_{11} = 3.8317$ (first node of the cylindrical Bessel function of order n=1),

$a = 10$ (radius of the cylinder, in kilometers),

$\theta = \frac{\pi}{2}$ (polar angle, which cannot be an integer multiple of π),

$L = 20$ (height of the cylinder, in kilometers)

$6 \le z \le 9$ (z measured in kilometers)

equation (35) becomes

$$\Psi(\rho,\theta,z) = [\sqrt{\frac{2}{\pi(3.8317)}} \cdot \cos(3.8317 - \frac{3\pi}{4})]\sin(\frac{\pi}{2})\sin(\frac{\pi}{20}z)\,. \tag{36}$$

Evaluation of k^2:

We evaluate k^2 using the values provided above:

$$k^2 = \alpha^2 + \gamma^2 = \frac{\chi_{ln}^{\,2}}{a^2} + \frac{n^2\pi^2}{L^2} = \frac{(3.8317)^2}{10^2} + \frac{\pi^2}{20^2} = 0.1714932599\,. \tag{37}$$

From the linkage equations (23) we have

$\lambda_i^2 = k^2 D + (1-\omega_0)K \cdot c\,.$

Substituting the values

$k^2 = 0.1714932599\,,$

$$D = \frac{c}{3K(1-g\omega_0)} = \frac{3\times10^8}{3(\frac{1}{16})\{1-(0.84)(0.9996)\}} \approx 9.979\times10^9\,, \tag{38}$$

into this equation, an estimate for λ_i^2 is obtained.

Evaluation of $\hat{\Omega}\cdot\nabla\Psi_{lmn}$:

We begin with equation (B.16) of Appendix B:

$$\hat{\Omega}\cdot\nabla\Psi_{lmn}(\vec{r}) = \{[-\sqrt{\frac{2a}{\pi\chi_{ln}\rho}}[\frac{\chi_{ln}}{a}\sin(\frac{\chi_{ln}}{a}\rho-\frac{3\pi}{4})]+\frac{1}{2\rho}\cos(\frac{\chi_{ln}}{a}\rho-\frac{3\pi}{4})]$$

$$\cdot\sin(m\theta)\sin(\frac{n\pi}{L}z)\sin\theta\}+\{\frac{n\pi}{L}\cos(\frac{n\pi}{L}z)\sin(m\theta)$$

$$\cdot\sqrt{\frac{2a}{\pi\chi_{ln}\rho}}\cos(\frac{\chi_{ln}}{a}\rho-\frac{3\pi}{4})\cos\theta\}. \tag{39}$$

Using the Bessel function of order 1, the first node $\chi_{11}=3.8317$, $m=n=1$,

$\rho=a=10\,\text{km}$ and $L=20\,\text{km}$, equation (39) becomes

$$\hat{\Omega}\cdot\nabla\Psi_{lmn}(\vec{r}) = \{[-\sqrt{\frac{2}{\pi\cdot 3.8317}}[\frac{3.8317}{10}\sin(3.8317-\frac{3\pi}{4})]+\frac{1}{2\cdot 10}\cos(3.8317-\frac{3\pi}{4})]$$

$$\cdot\sin(\frac{\pi}{2})\sin(\frac{\pi}{20}z)\sin(\frac{\pi}{2})\}+\{\frac{\pi}{20}\cos(\frac{\pi}{20}z)\sin(\frac{\pi}{2})$$

$$\cdot\sqrt{\frac{2}{\pi\cdot 3.8317}}\cos(3.8317-\frac{3\pi}{4})\cos(\frac{\pi}{2})\} \tag{40}$$

Since $\cos\frac{\pi}{2}=0$, equation (40) reduces to

$$\hat{\Omega}\cdot\nabla\Psi_{lmn}(\vec{r}) = \{[-\sqrt{\frac{2}{\pi\cdot 3.8317}}[\frac{3.8317}{10}\sin(3.8317-\frac{3\pi}{4})]+\frac{1}{2\cdot 10}\cos(3.8317-\frac{3\pi}{4})]$$

$$\cdot\sin(\frac{\pi}{2})\sin(\frac{\pi}{20}z)\sin(\frac{\pi}{2})\}. \tag{41}$$

Evaluation of the Intensity:

The intensity distribution in cylindrical coordinates is given by

$$I(\vec{r},\hat{\Omega},t)=\frac{{\chi_{ln}}^{2}}{a^{2}\pi L\cdot[\sin(\chi_{ln}-\frac{3\pi}{4})+2\chi_{ln}-1]}\cdot$$

$$\sum_{l=1}^{\infty}\sum_{m=1}^{\infty}\sum_{n=1}^{\infty}\Psi_{lmn}(\vec{r})-\frac{3D}{c}\hat{\Omega}\cdot\nabla\Psi_{lmn}(\vec{r})][\sum_{j=1}^{N}\omega_{j}\Psi_{lmn}(\vec{r}_{j})e^{-\lambda_{lmn}^{2}(t-t_{j})}], \tag{42}$$

which is modified to

$$I(\vec{r},\hat{\Omega},t)=\frac{{\chi_{ln}}^{2}}{a^{2}\pi L\cdot[\sin(\chi_{ln}-\frac{3\pi}{4})+2\chi_{ln}-1]}\cdot\sum_{l=1}^{\infty}\sum_{m=1}^{\infty}\sum_{n=1}^{\infty}J_{n}(\frac{\chi_{ln}}{a}\rho)\sin(n\theta)\sin(\frac{m\pi}{L}z)-\frac{3D}{c}\cdot$$

$$\{[-\sqrt{\frac{2a}{\pi\chi_{nl}\rho}}[\frac{\chi_{nl}}{a}\sin(\frac{\chi_{nl}}{a}\rho-\frac{3\pi}{4})]+\frac{1}{2\rho}\cos(\frac{\chi_{nl}}{a}\rho-\frac{3\pi}{4})]\sin(m\theta)\sin(\frac{n\pi}{L}z)\cdot\sin\theta\}+\{$$

$$\frac{n\pi}{L}\cos(\frac{n\pi}{L}z)\sin(m\theta)\sqrt{\frac{2a}{\pi\chi_{nl}\rho}}\cos(\frac{\chi_{nl}}{a}\rho-\frac{3\pi}{4})\cdot\cos\theta\}\cdot[\sum_{j=1}^{N}\omega_{j}\Psi_{lmn}(\vec{r}_{j})e^{-\lambda_{lmn}^{2}(t-t_{j})}]. \tag{43}$$

Continuing with the simplifications and substitution of constants, equation (43) becomes

$$I(\vec{r},\hat{\Omega},t)=\frac{{\chi_{ln}}^{2}}{a^{2}\pi L\cdot[\sin(\chi_{ln}-\frac{3\pi}{4})+2\chi_{ln}-1]}\cdot$$

$$\sum_{l=1}^{\infty}\sum_{m=1}^{\infty}\sum_{n=1}^{\infty}[\sqrt{\frac{2}{\pi\frac{\chi_{nl}}{a}\rho}}\cos(\frac{\chi_{nl}}{a}\rho-\frac{3\pi}{4})]\sin(n\theta)\sin(\frac{m\pi}{L}z)-\frac{3D}{c}\cdot\{[$$

$$-\sqrt{\frac{2a}{\pi\chi_{nl}\rho}}[\frac{\chi_{nl}}{a}\sin(\frac{\chi_{nl}}{a}\rho-\frac{3\pi}{4})]+\frac{1}{2\rho}\cos(\frac{\chi_{nl}}{a}\rho-\frac{3\pi}{4})]\sin(m\theta)\sin(\frac{n\pi}{L}z)\cdot\sin\theta\}+\{$$

$$\frac{n\pi}{L}\cos(\frac{n\pi}{L}z)\sin(m\theta)\sqrt{\frac{2a}{\pi\chi_{nl}\rho}}\cos(\frac{\chi_{nl}}{a}\rho-\frac{3\pi}{4})\cdot\cos\theta\}\cdot[\sum_{j=1}^{N}\omega_{j}\Psi_{lmn}(\vec{r}_{j})e^{-\lambda_{lmn}^{2}(t-t_{j})}]. \tag{44}$$

Working similarly as in [1], we truncate the series by retaining only the terms with $l=m=n=1$. Using the Bessel function of order 1, first node $\chi_{11}=3.8317$ and $\rho=a=10\,\text{km}$, $L=20\,\text{km}$ leads to the required approximation for the intensity of radiation as

$$\begin{aligned}
I(\vec{r},\hat{\Omega},t) = {} & \frac{(3.8317)^2}{10^2\pi\cdot 20\cdot[\sin(3.8317-\frac{3\pi}{4})+2(3.8317)-1]}\cdot \\
& [\sqrt{\frac{2}{\pi(3.8317)}}\cos(3.8317-\frac{3\pi}{4})]\sin(\frac{\pi}{2})\sin(\frac{\pi}{20}z)-\frac{3D}{c}\cdot \\
& \{[-\sqrt{\frac{2}{\pi(3.8317)}}[\frac{3.8317}{10}\sin(3.8317-\frac{3\pi}{4})]+\frac{1}{2\cdot 10}\cos(3.8317-\frac{3\pi}{4})] \\
& \sin(\frac{\pi}{2})\sin(\frac{\pi}{20}z)\cdot\sin(\frac{\pi}{2})\}\cdot[\sum_{j=1}^{N}\omega_j\Psi_{111}(\vec{r}_j)e^{-\lambda_{lmn}^2(t-t_j)}].
\end{aligned} \tag{45}$$

In equation (45), the term $\Psi_{111}(\vec{r}_j)e^{-\lambda_{lmn}^2(t-t_j)}$ corresponds to the 61 point sources animating the cylindrical cloud. Please note that $\Psi_{111}(\vec{r}_j)$ is evaluated at $\vec{r}_j$, which is the location of the lightning source and not that of the observer located at $\vec{r}$.

5.2 Graphical representations

Once numerical values of the constants present in the code have been provided, the numerical simulations used in this thesis generate a near realistic cloud from which to evaluate lightning intensity. The 61 point sources located at r_j animate the cloud. To visualize the output, we plot the intensity of the radiation of lightning versus time. In what follows, different angles, mean free paths and cloud sizes have been selected. The following figures are provided to justify the claim. This section will be divided into three parts (a, b, c). Section 5.2 a) begins with the display of Figure 6.

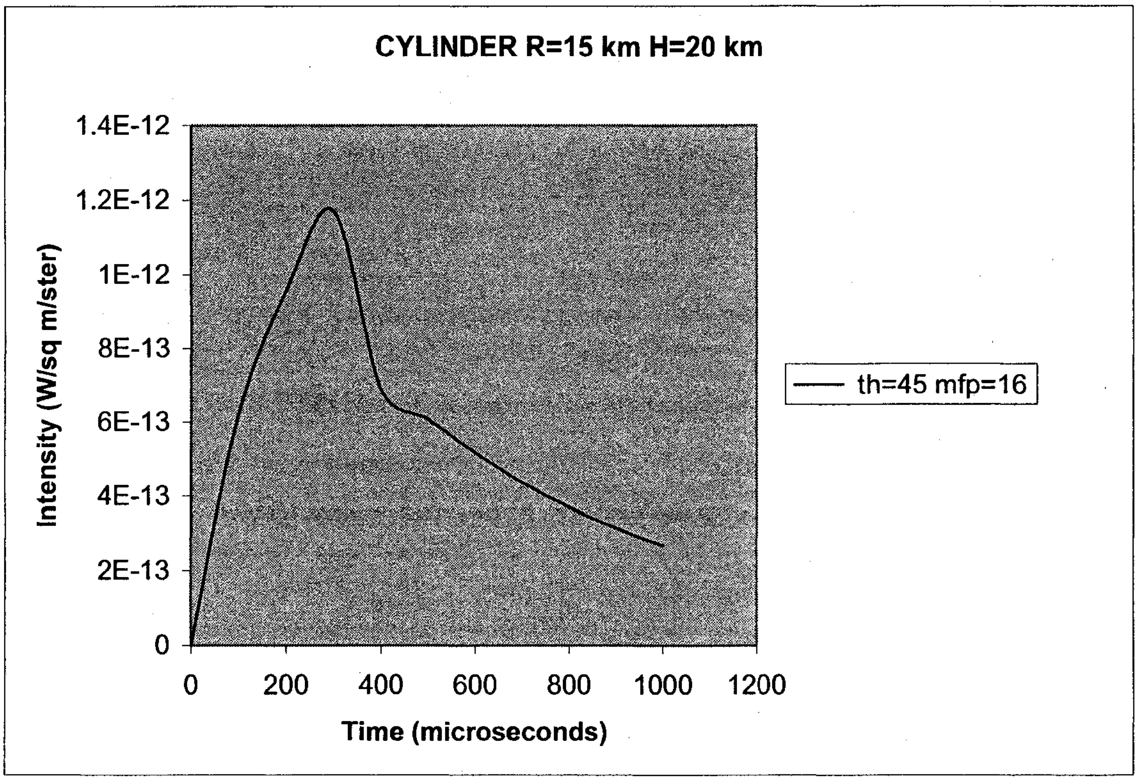

Figure 6

In Figure 6, the intensity of the propagation of radiation through the cylindrical cloud due to lightning is displayed with respect to time. In this graph, the polar angle θ is chosen to be 45^o. The x and y coordinates, the horizontal extent of the channel of propagation, are each held constant at 5 km. The z coordinate is allowed to vary from 6 km to 9 km. The purpose of selecting 6-9 km is for comparison purposes with reference [1]. The x, y and z coordinates represent the locations of the 61 point sources. The z coordinates vary at increments of 50 meters each. Time is measured in microseconds (μs), whereas the intensity is measured in W/m^2/steradians. In Figure 6, the model produces a peak amplitude of 1.17 E-12 W/m^2/steradians associated with significant time width. For this plot, a cylinder with a radius of 15 km and a height of 20 km was used. The mean free path was chosen to be 16.

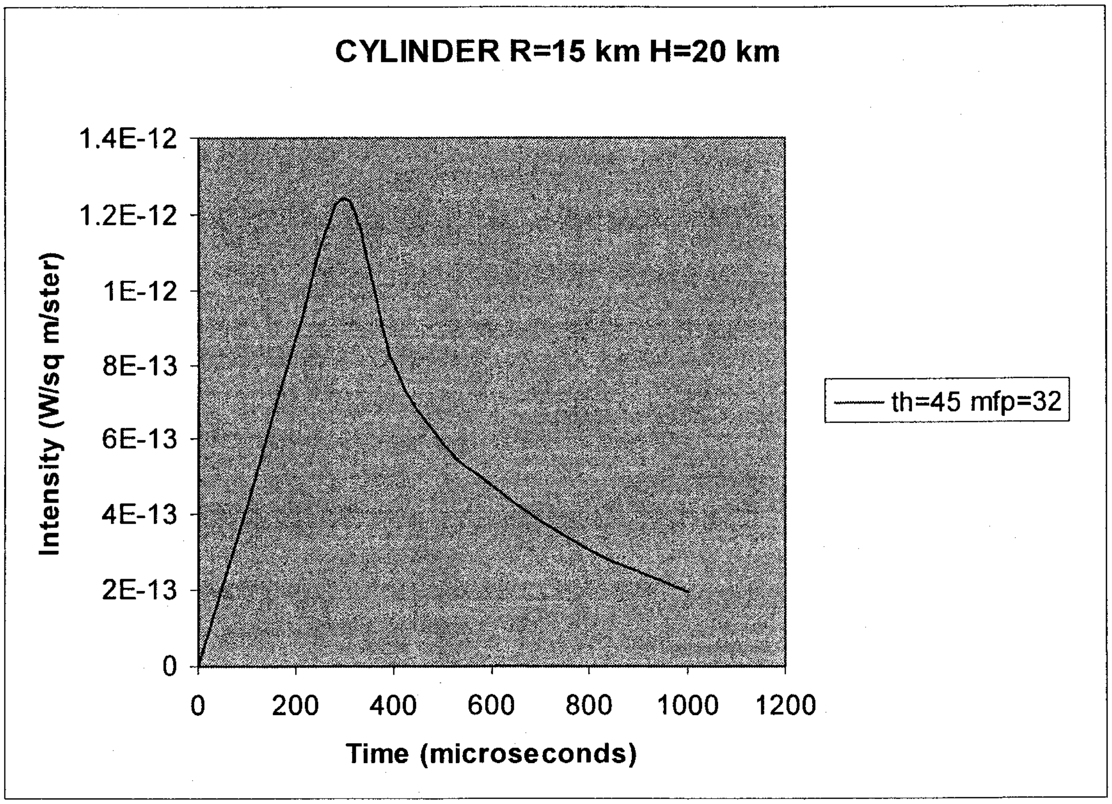

Figure 7

In Figure 7, the same geometric constraints as in Figure 6 are preserved. The polar angle remains invariant, but the mean free path has been allowed to increase to 32. The main difference between Figure 6 and Figure 7 is in the peak intensity, which is higher in Figure 7. This difference is more apparent when Figure 6 and Figure 7 are superimposed to produce Figure 8.

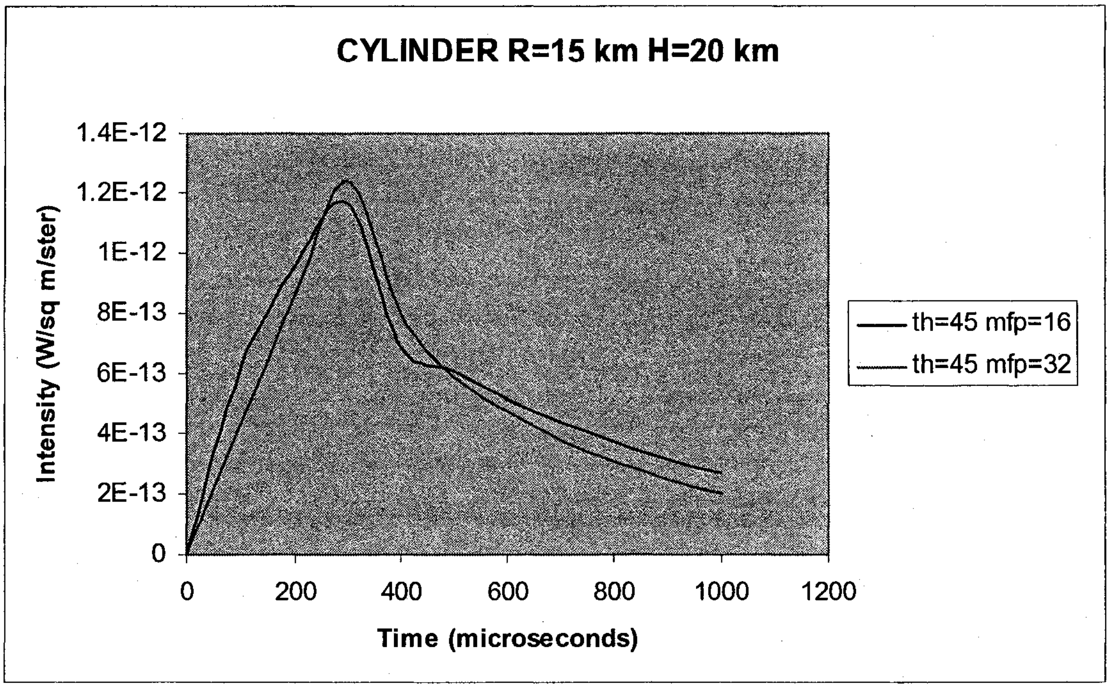

Figure 8

The next set of Figures: (9, 10, 11), corresponds to a cylinder of radius r=15 km and height h=20 km. The same mean free paths (16 and 32) are utilized. The primary change in this set of figures is that the angle of observation changes from 45^o to 90^o.

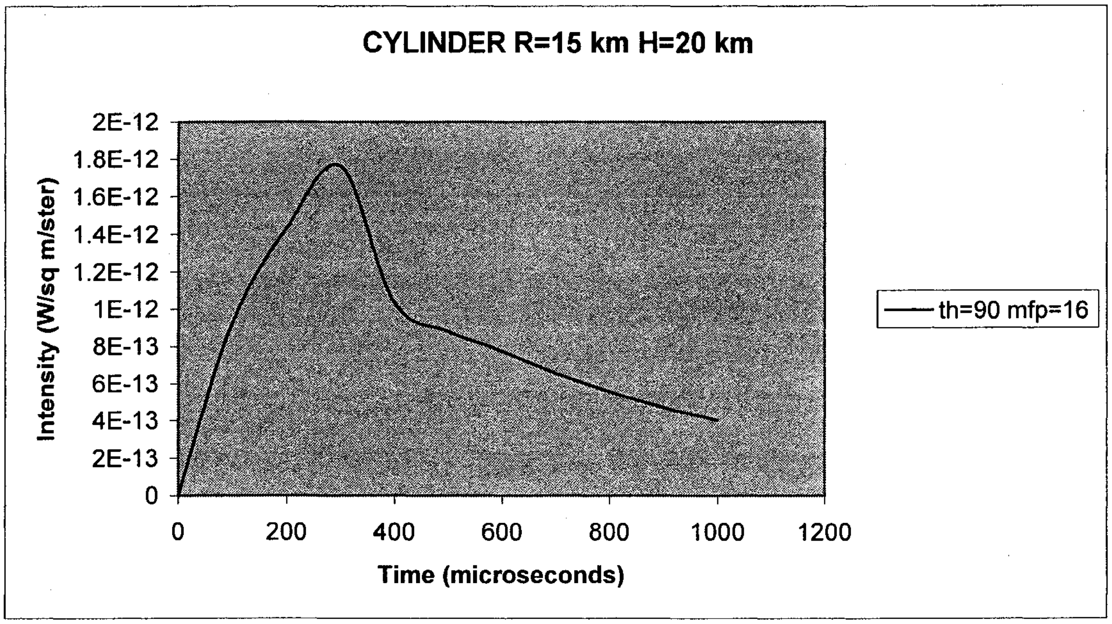

Figure 9

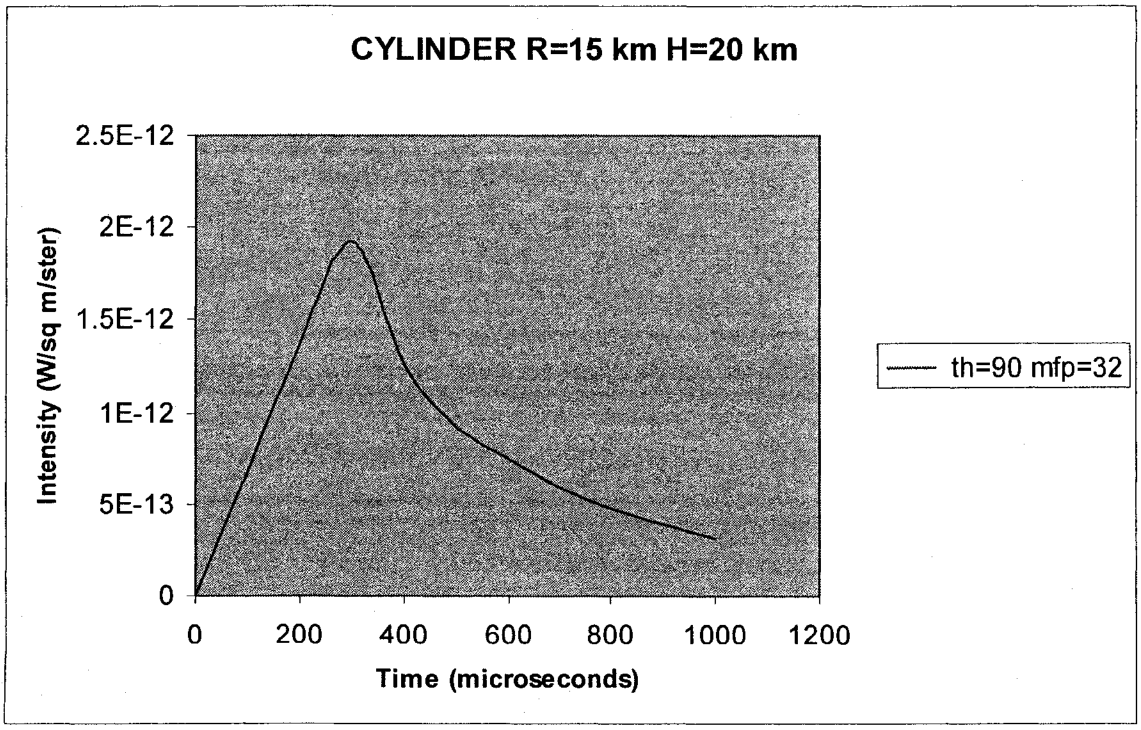

Figure 10

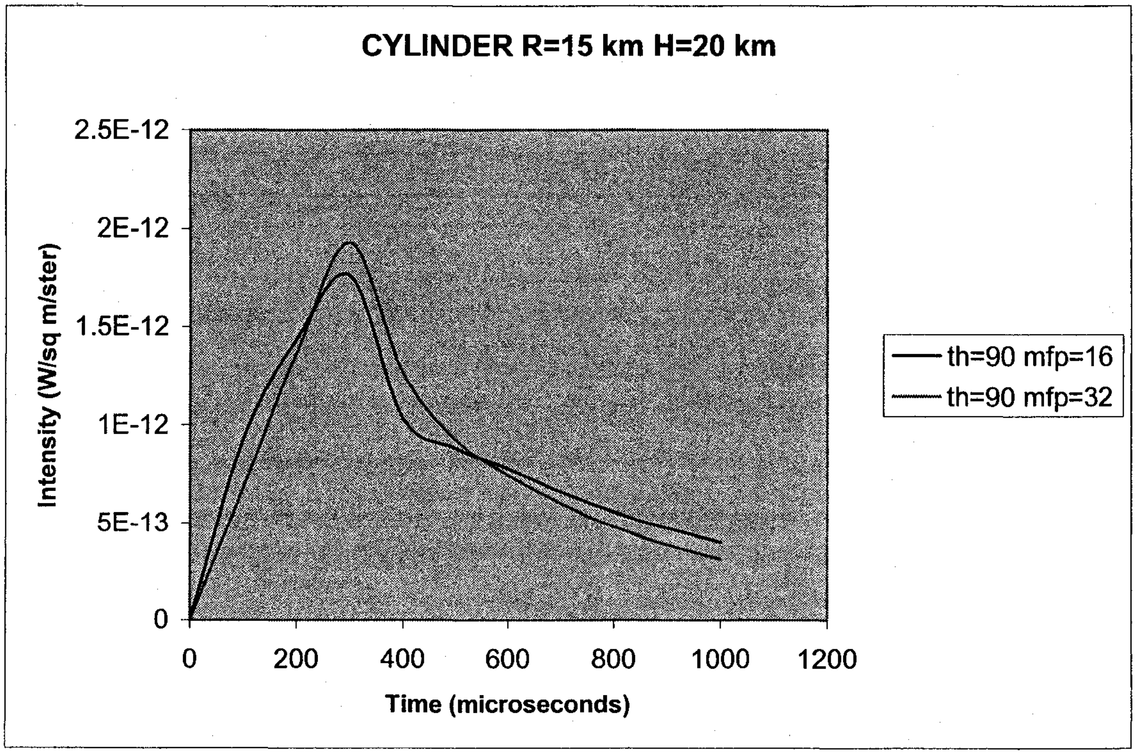

Figure 11

As in the previous set (Figures 6, 7 and 8), the graphs corresponding to the larger mean free path displays a larger peak intensity. Figure 11 is a superposition of Figures 9 and 10. In addition, the peak intensities for the graphs with observation angle $\theta = 90^o$ are higher than those at $\theta = 45^o$.

Section 5.2b): Figures 12-17 comprise a set of graphs where the radius of the cylinder has shrunk to 12 km but the same height of 20 km is preserved. Also, the same mean free paths 16, 32 are kept, as are the two angles of observation $\theta = 45^o$ and $\theta = 90^o$. As above, the graphs corresponding to the larger mean free path display a higher peak intensity.

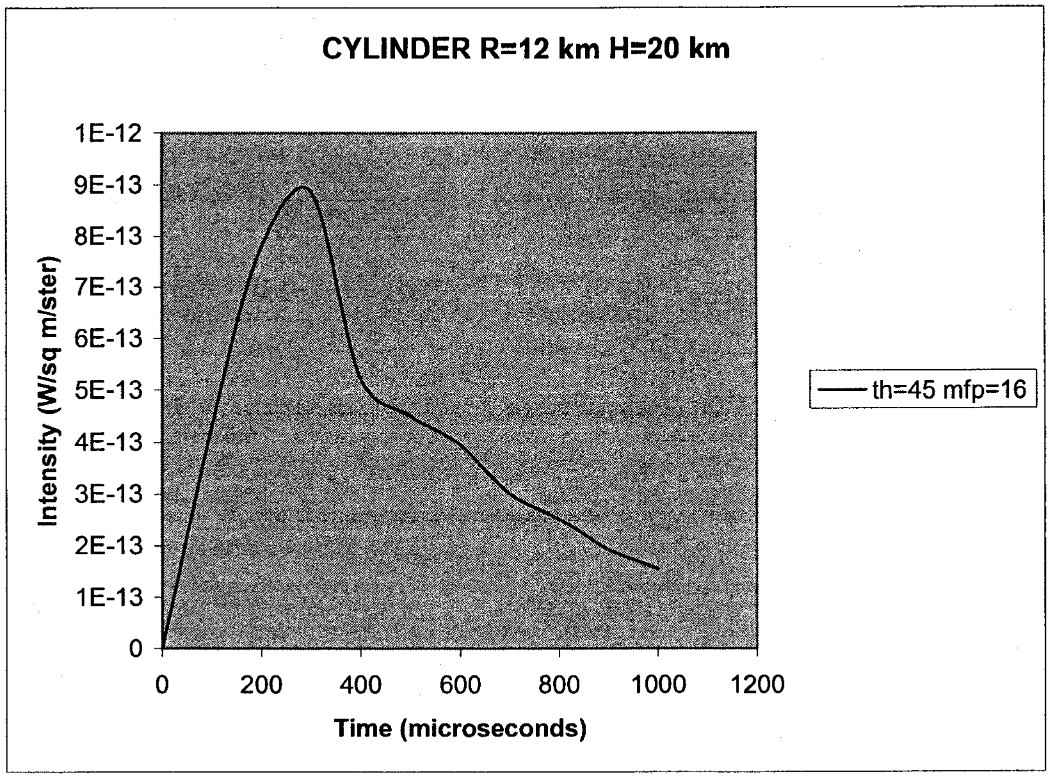

Figure 12

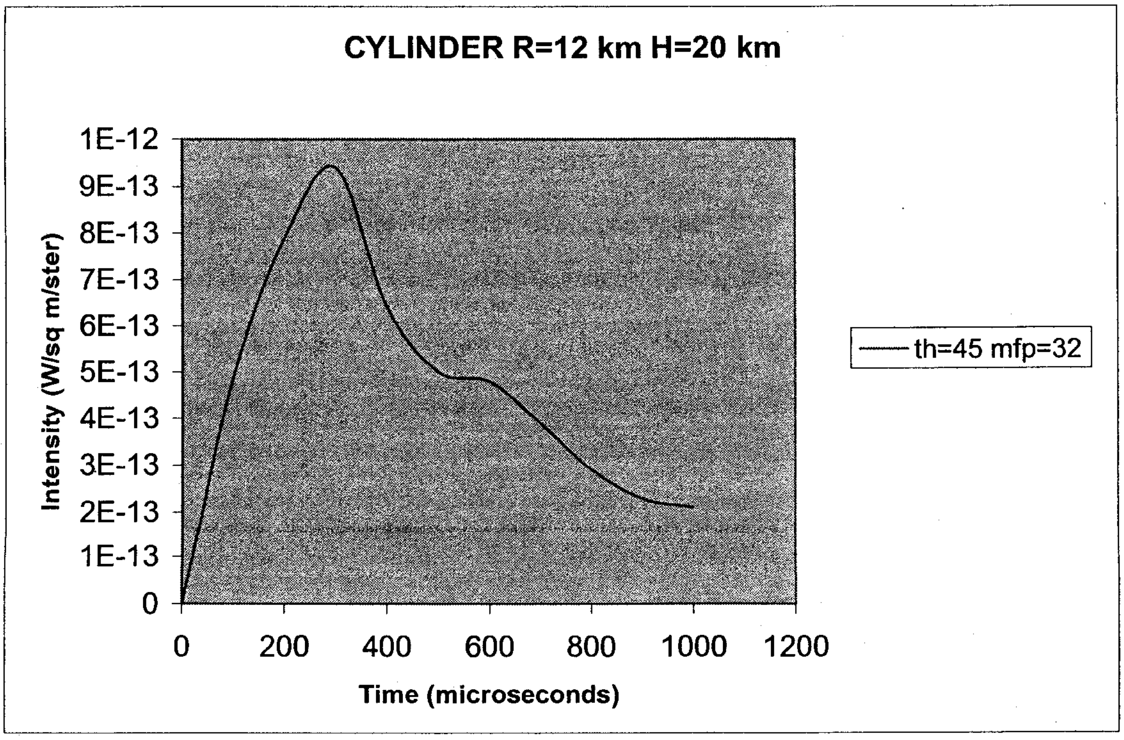

Figure 13

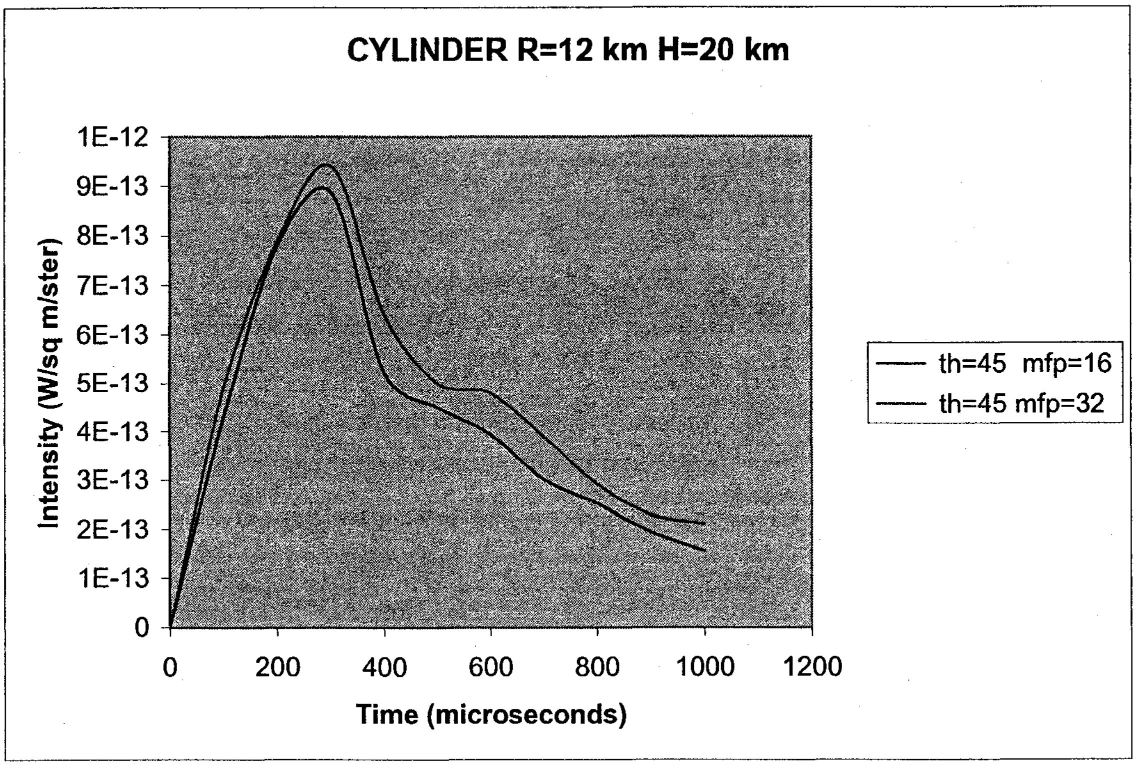

Figure 14

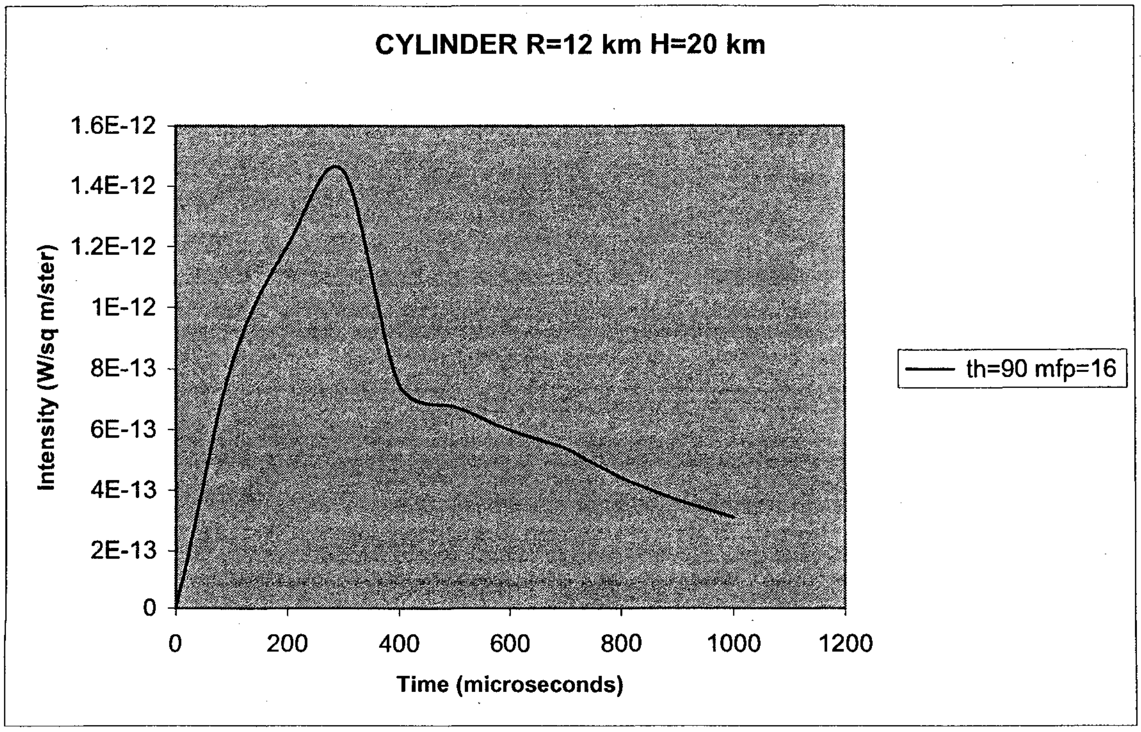

Figure 15

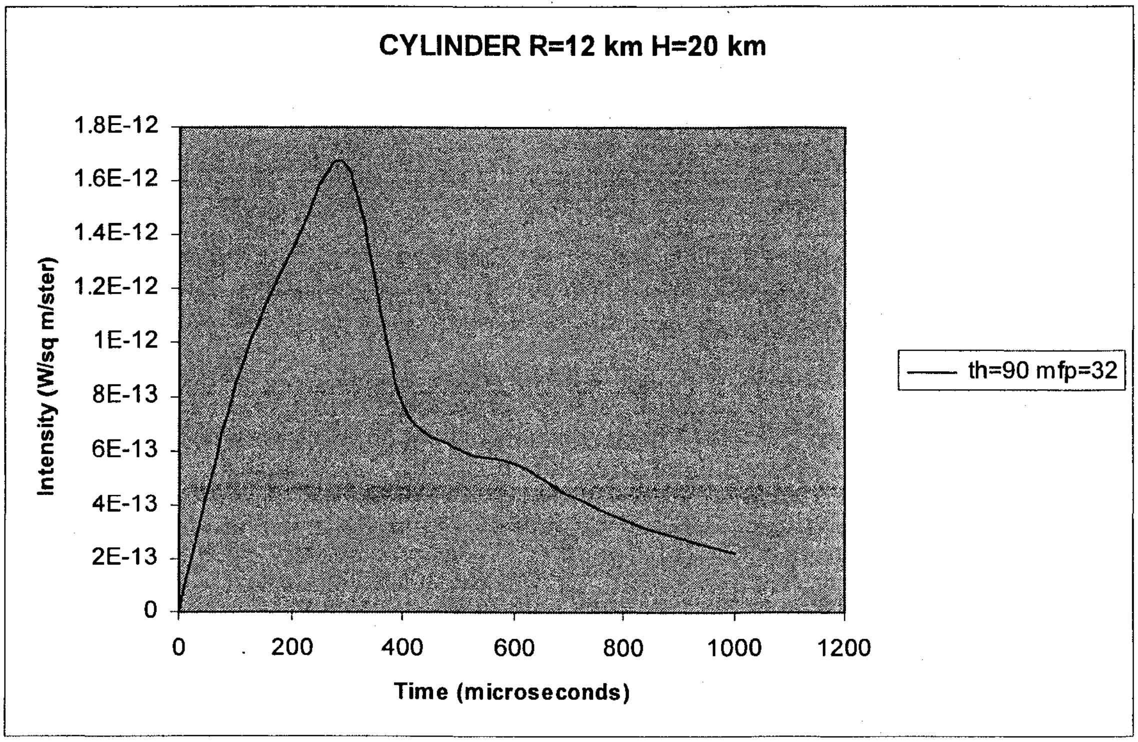

Figure 16

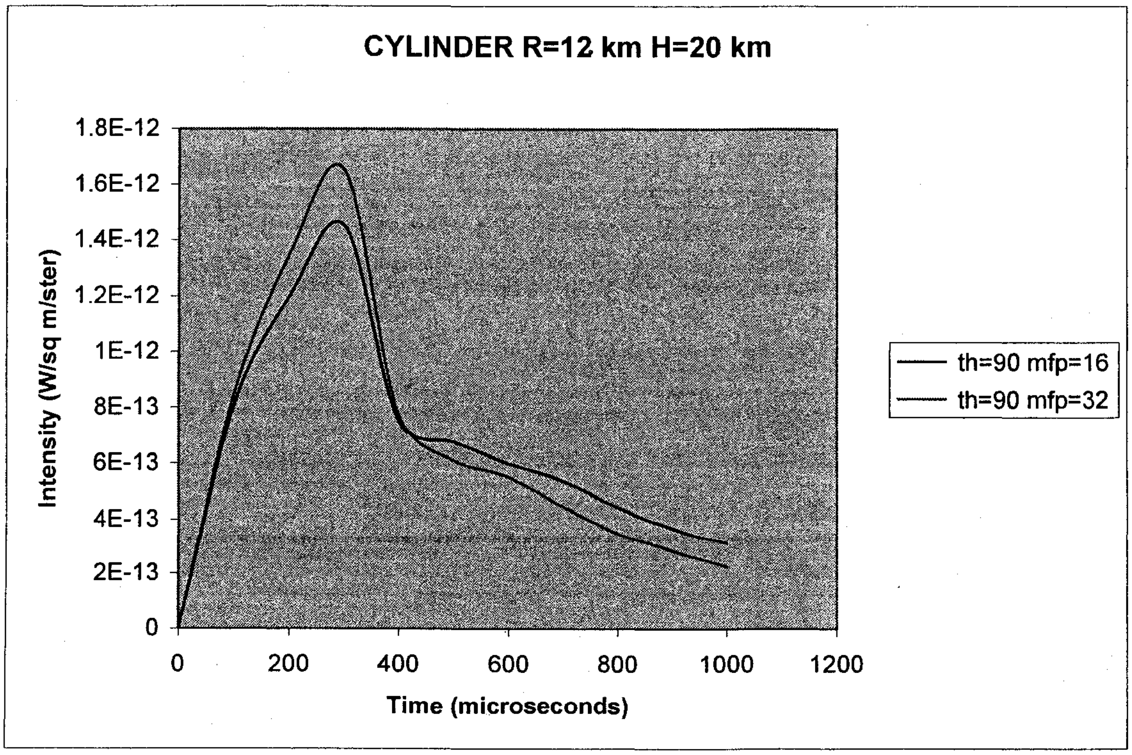

Figure 17

As in section 5.2a, Figures 14 and 17 are obtained by superimposing Figures (12, 13) and (15, 16), respectively. Also, the graphs corresponding to the angle of observation $\theta = 90^o$ displayed higher intensities than those viewed at $\theta = 45^o$. Moreover, the decrement in the radius of the cylinder shrinks its volume, thereby reducing the peak intensities.

Section 5.2c): In this section, the radius of the cylinder is shrunk to $r = 10$ km. The height of 20 km is preserved, and only one angle of observation $\theta = 45^o$ is used. Also, the two mean free paths 16 and 32 are kept.

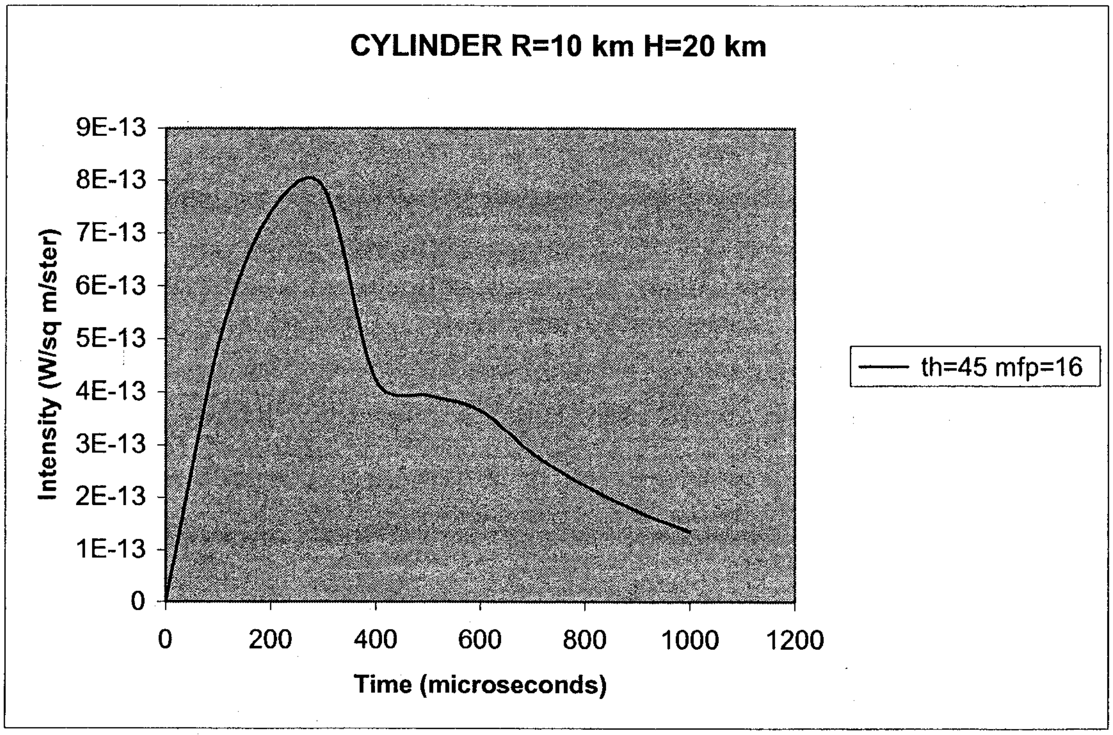

Figure 18

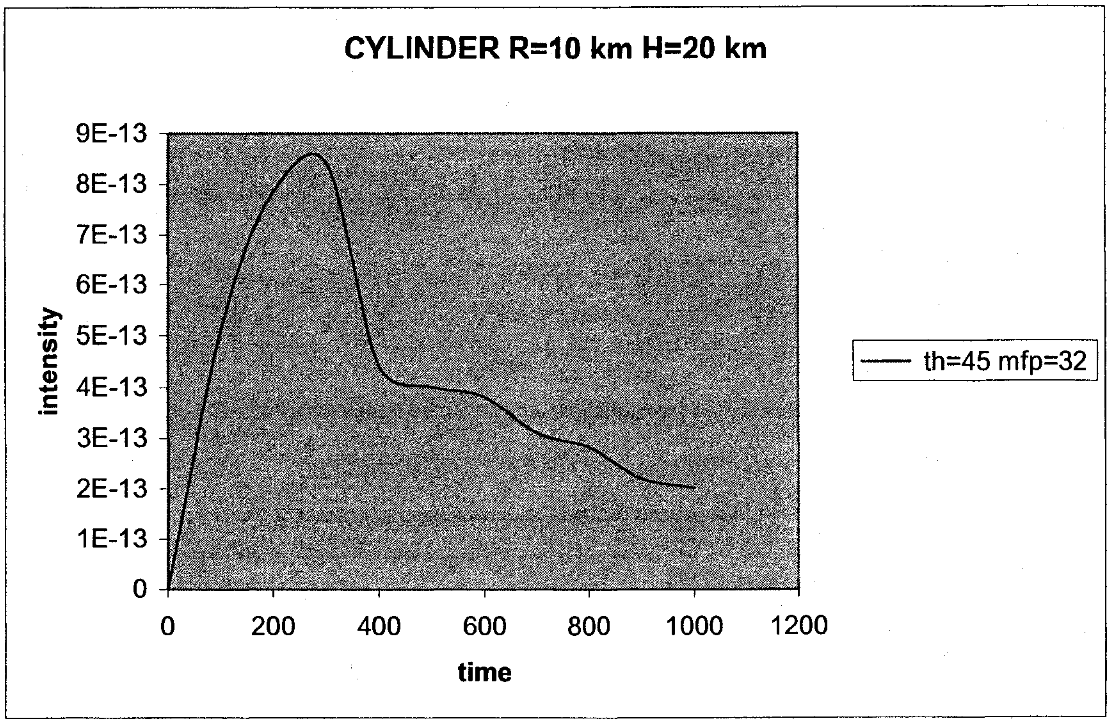

Figure 19

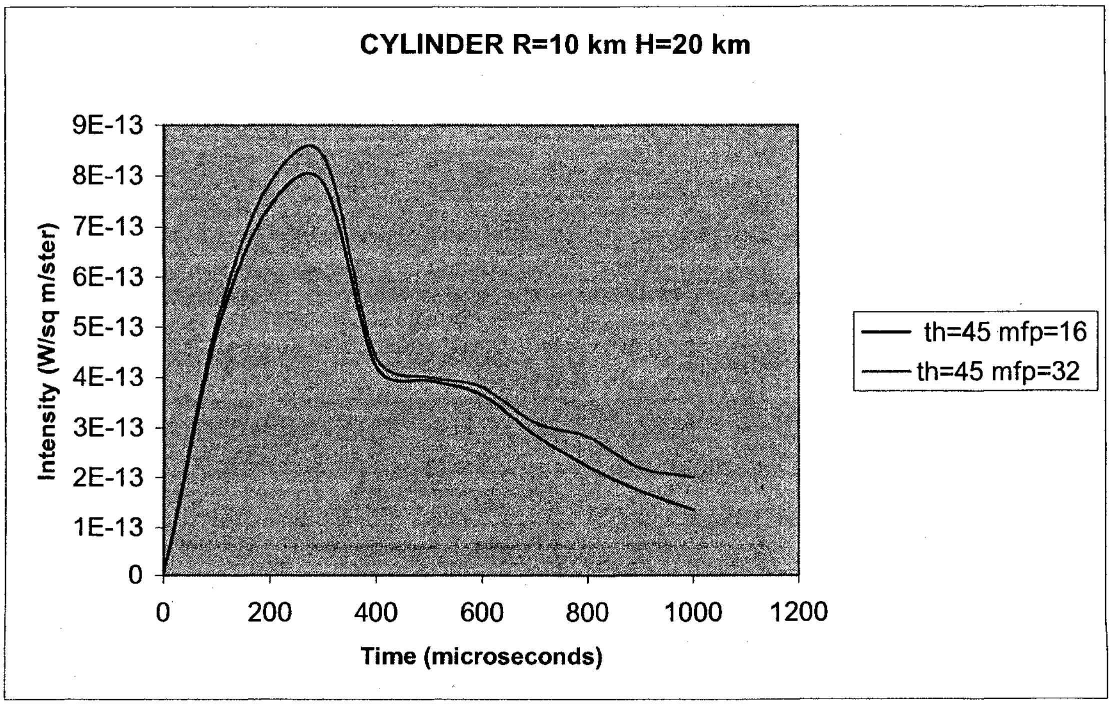

Figure 20

As with the previous cases, the graph with the mean free path of 32 is dominant.

5.3 Analysis of Results

In the 16 graphs provided above, the following observations can be made when the mean free paths, the polar angles and the sizes of the cylindrical cloud are allowed to vary.

Section 5.3a): Influence of the Mean Free Path. The numerical calculations utilized two different mean free paths, 16 and 32. When the mean free path is small, and the same number density is present, the probability of photon collisions increases. When photons undergo more collisions, the process exhibits a larger multiple scattering effect, which affects the intensity of the propagation of radiation. So the graphs associated with the mean free path of 16 display smaller peak intensities than those corresponding to the mean free path of 32.

Section 5.3b): Influence of the Polar Angle. The polar angle plays a role in defining the extent of the channel of propagation of lightning events. The angle is also used to describe the events, as well as to describe the tortuosity of the channel. In different milieux, it is understood as additional opposition or difficulty in the propagation of the intensity of radiation. When the polar angle is set at $\theta = 45^o$, the horizontal extent of the channel affects the peak intensity more profoundly in a negative way than at $\theta = 90^o$. When the polar angle is set at $\theta = 90^o$, the channel has a positive effect on the intensity of propagation. This is why the graphs corresponding to $\theta = 90^o$ are dominant and show faster risetime.

Section 5.3c) Influence of Size. It is expected that the dimensions of the cylinder play a role in the value of the intensity of propagation of radiation. Given the fact that the same number density is used, the larger the cylinder is, the more dilute it will be. Therefore, the photons present in the cloud involved will be engaged in a smaller number of collisions due to the excess volume. With a larger mean free path and a sizable volume, the value of the intensity of radiation is expected to increase. The reverse is also true. By shrinking the volume of the cylinder, its intensity is expected to decrease. These effects are evidenced in Figures 13 through 20. Figure 28, which will be discussed in Chapter 6, is unique, since equating the radius to the height of the cylinder coupled with a polar angle of 90^o provides an excellent channel of propagation for the intensity of radiation. The tables below provide a summary of the above analysis.

Table 1: $\theta = 45^o$ ***and*** $mfp = 16$

Radius (km)	Height (km)	Volume (km^3)	Number Density/ cm^3	Peak intensity ($W/m^2/ster$)	Vol. ratio (compared to radius 15km, height 20km)
15	20	14137.2	100	1.17E-12	1
12	20	9047.8	100	8.86E-13	0.640
10	20	6283.2	100	7.86E-13	0.444

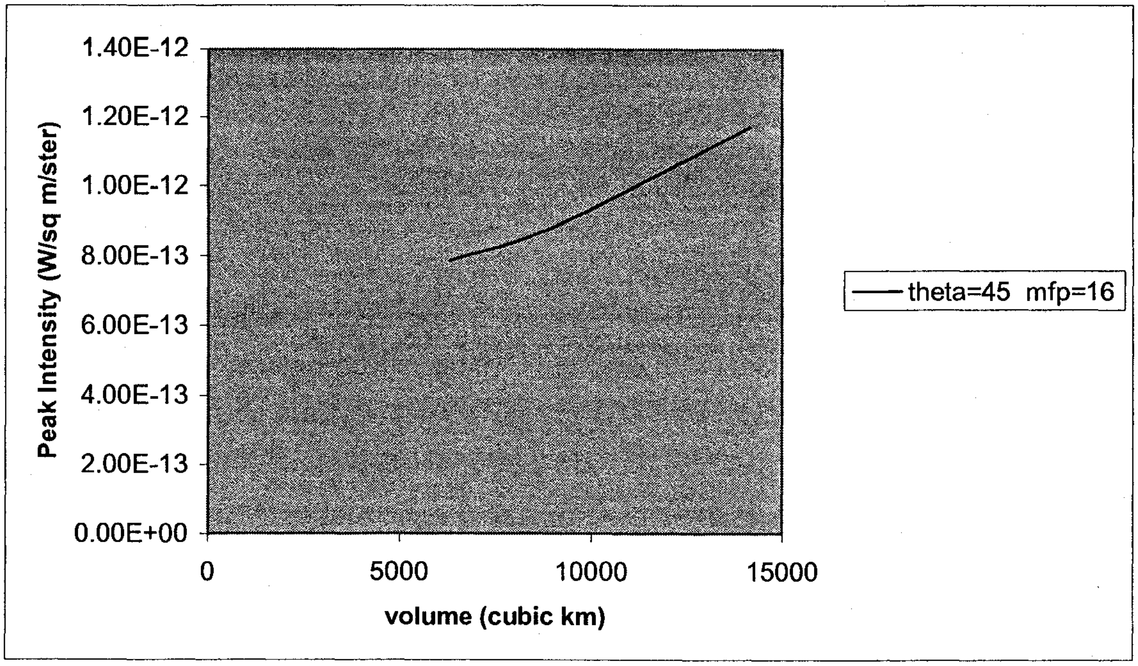

Figure 21

Table 2: $\theta = 45^{\circ}$ ***and*** $mfp = 32$

Radius (km)	Height (km)	Volume (km^3)	Number Density/ cm^3	Peak intensity (W/m^2/ster)	Vol. ratio (compared to radius 15km, height 20km)
15	20	14137.2	100	1.24E-12	1
12	20	9047.8	100	9.40E-13	0.640
10	20	6283.2	100	8.40E-13	0.444

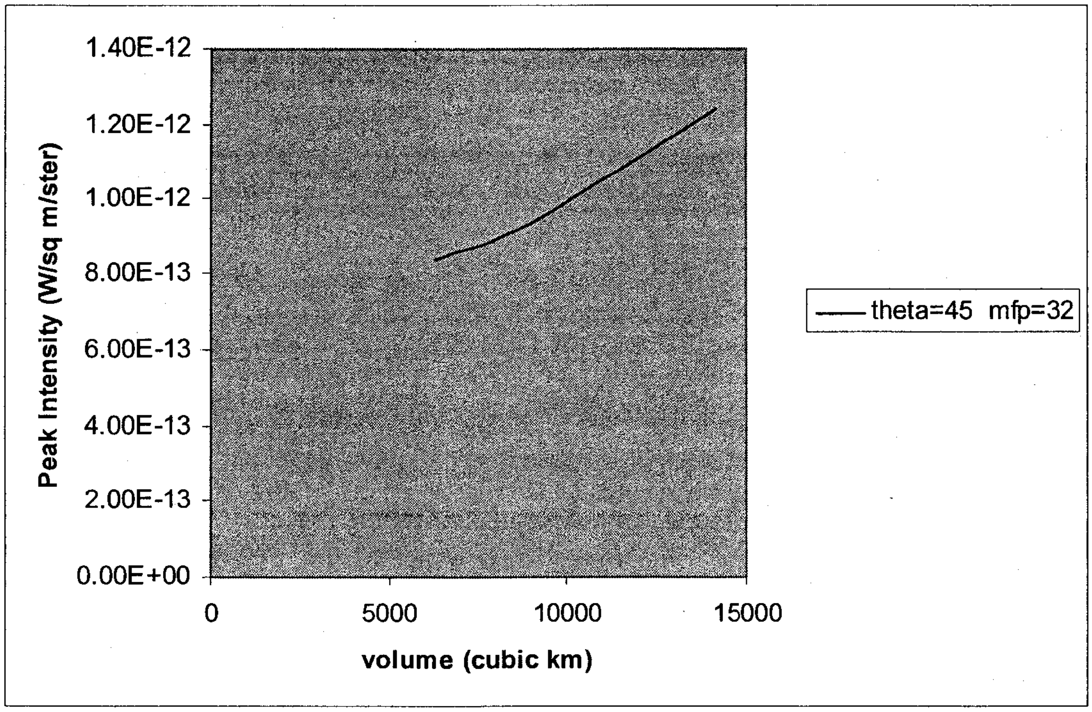

Figure 22

Table 3: $\theta = 90^o$ ***and*** $mfp = 16$

Radius (km)	Height (km)	Volume (km^3)	Number Density/ cm^3	Peak intensity ($W/m^2/ster$)	Vol. ratio (compared to radius 15km, height 20km)
15	20	14137.2	100	1.76E-12	1
12	20	9047.8	100	1.45E-12	0.640

Table 4: $\theta = 90^o$ ***and*** $mfp = 32$

Radius (km)	Height (km)	Volume (km^3)	NumberDensity/ cm^3	Peak intensity ($W/m^2/ster$)	Vol. ratio (compared to radius 15km, height 20km)
15	20	14137.2	100	1.93E-12	1
12	20	9047.8	100	1.65E-12	0.640

The result presented in the tables and plots above correspond to the appropriate physics which regulate the lightning phenomenon.

CHAPTER 6

COMPARISONS AND FUTURE WORK

The purpose of this chapter is to compare the work done in this thesis with both references [1] and [2], which used the "Diffusion Model for Lightning Radiative Transfer" adapted to a rectangular parallelepiped and a sphere, respectively. In contrast, a cylindrical geometry was used in this study. The same codes originated from [1] were utilized in the three studies and the same required numerical values of the physical constraints c, g, λ, ω_o were preserved. To assist in the comparisons, several graphs are provided. The polar angle $\theta = 45^o$ associated with two different mean free paths of 16 and 32 is selected. The cases to be considered are described below:

(a) a cube of dimensions $a = b = c = 10\,\text{km}$;

(b) a sphere of radius $r = 17.3\,\text{km}$; and

(c) a circular cylinder of radius $r = 15\,\text{km}$ and height $h = 20\,\text{km}$;

(d) a modified cylinder of equal height and radius ($r = h = 7\,\text{km}$) with a polar angle $\theta = 90^o$.

6.1 Comparisons

We begin by displaying the relevant graphs.

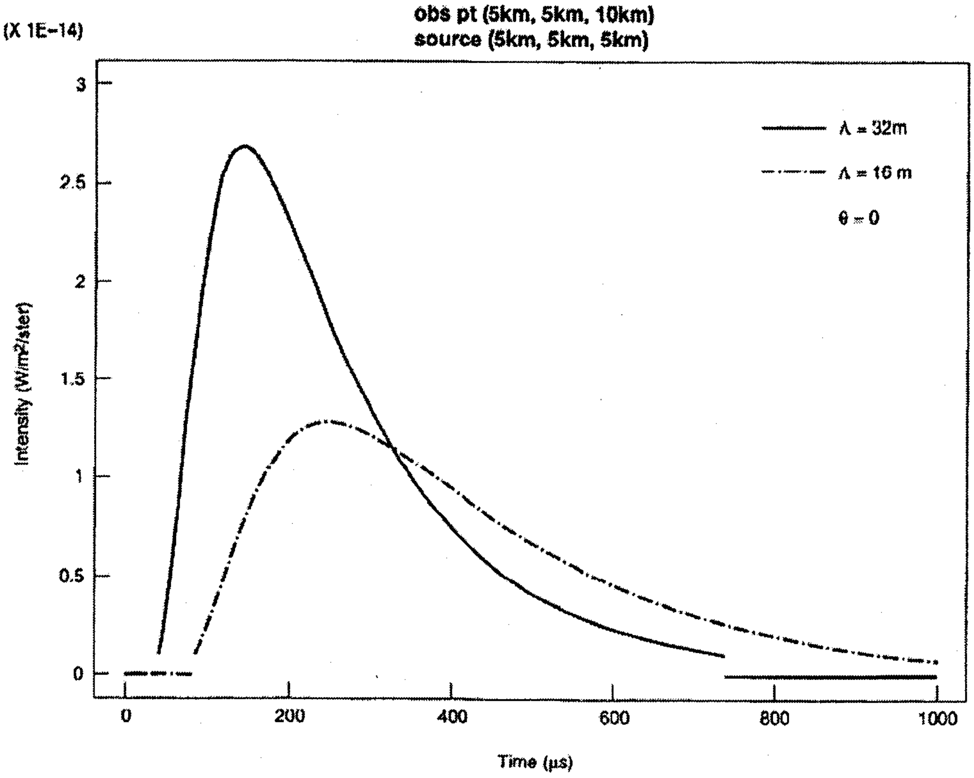

Figure 23: Effect of cloud optical thickness on a transient point source located at the center of a cubic cloud (dimension = 10 km). Detector is at or above the center of the cloud top and is looking down. Note that the "thicker" cloud (smaller mean free path) time delays and time broadens the source more, as expected. The sharp breaks in the intensity curve at about 100 and 750 μs *indicate when acceptable truncation error thresholds are met.*

Figures 24 and 26 below are from reference [2], whereas Figures 25 and 27 are generated by the cylindrical model.

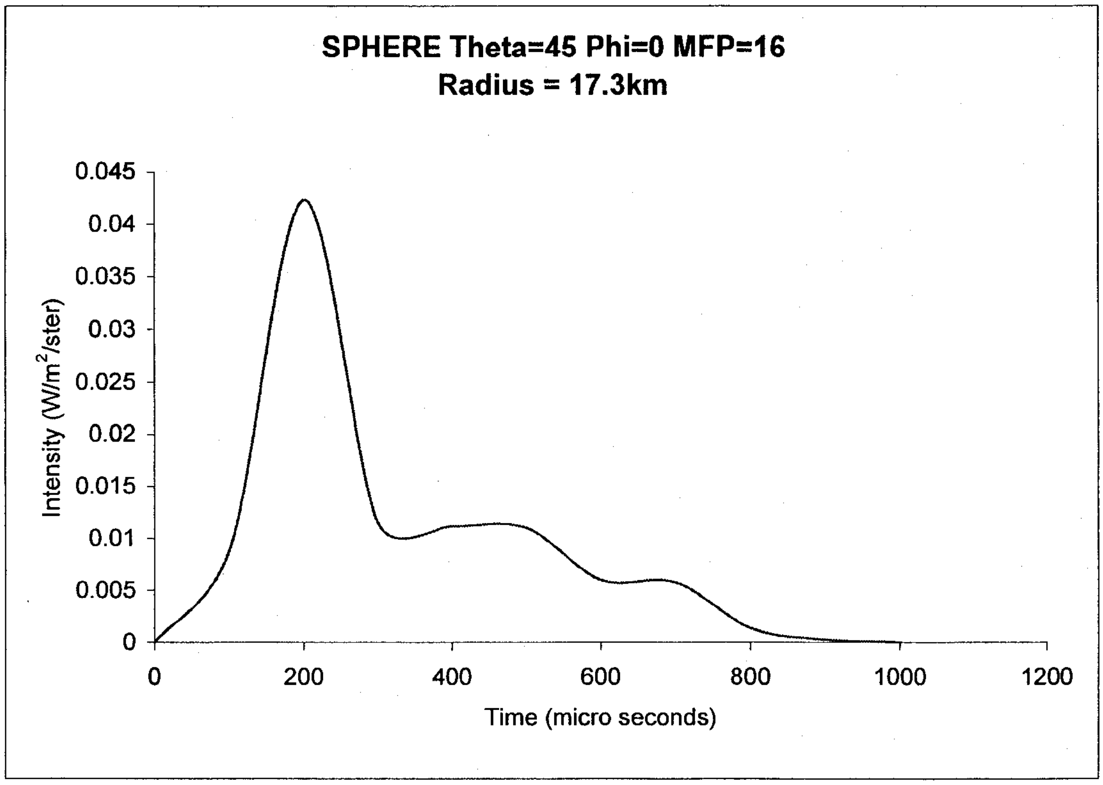

Figure 24

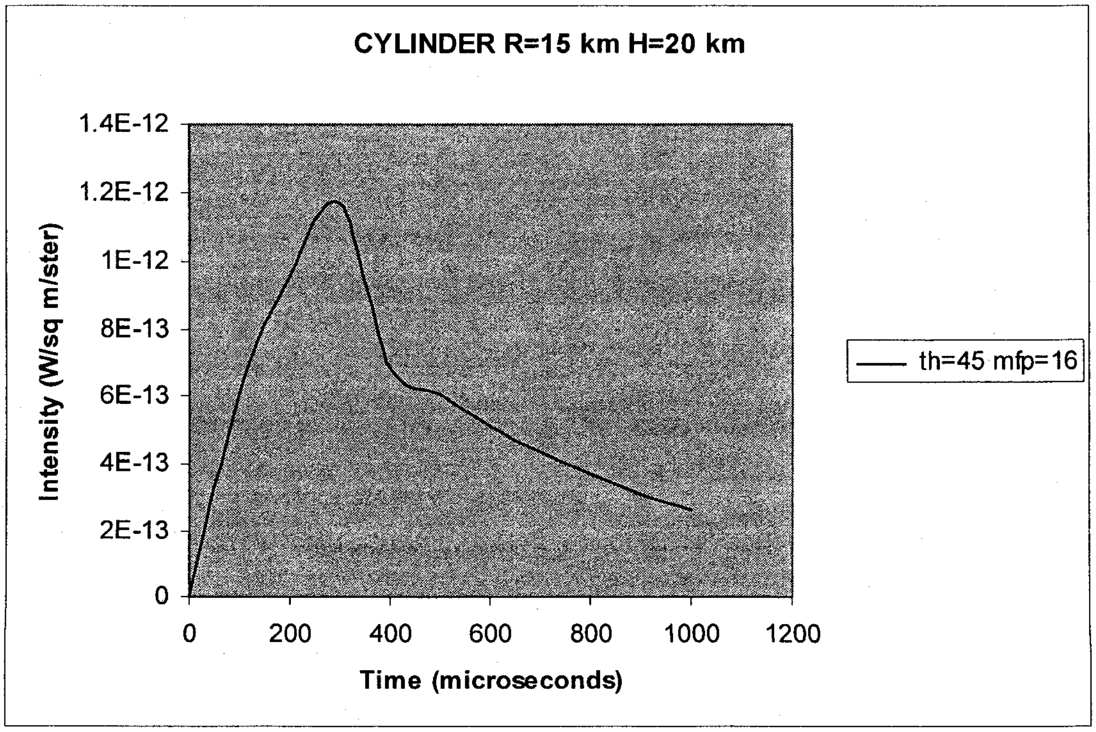

Figure 25

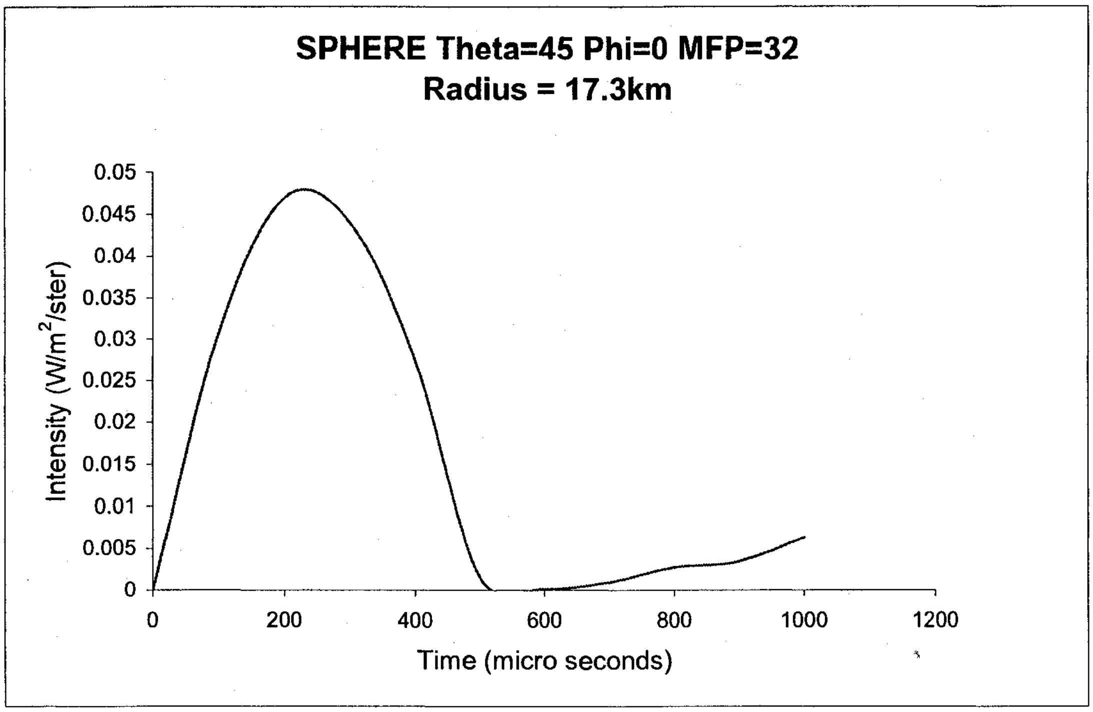

Figure 26

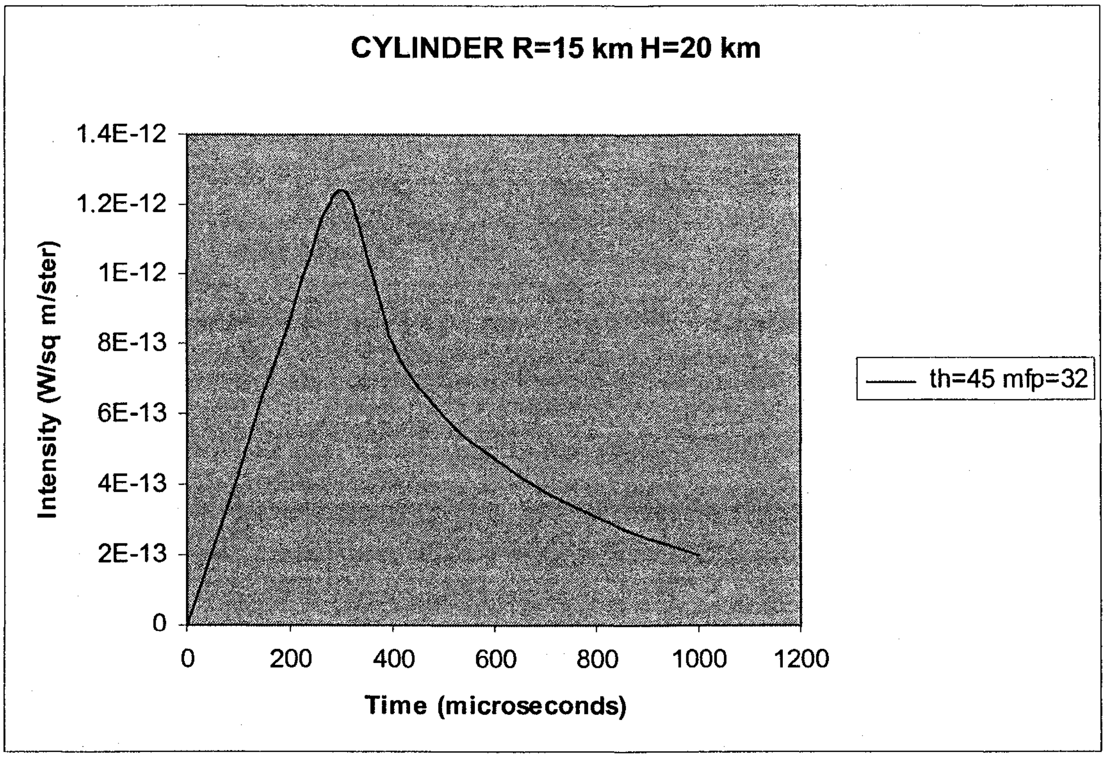

Figure 27

The results of these graphs are summarized in the two tables given below:

Table 5:

	Dimensions (km)	Polar angle (degrees)	Azimuthal angle (degrees)	Mean Free Path (m)	Density/cm^3	Volume (km^3)	Peak value of Intensity of radiation
Cube	$a=b=c=10$	0		16	100	1000	1.28E-14
Sphere	Radius=17.3	45	0	16	100	21688.4	0.0423
Cylinder	Radius = 15, Height = 20	45		16	100	14137.2	1.17E-12

Table 6:

	Dimensions (km)	Polar angle (degrees)	Azimuthal angle (degrees)	Mean Free Path (m)	Density/cm^3	Volume (km^3)	Peak value of Intensity of radiation
Cube	$a=b=c=10$	0		32	100	1000	2.70E-14
Sphere	Radius=17.3	45	0	32	100	21688.4	0.047
Cylinder	Radius = 15, Height = 20	45		32	100	14137.2	1.24E-12

In all these cases, the spherical model is dominant. This is expected, since it covers a much larger volume than the cube or cylinder. The most interesting comparisons are between the cylinder and the rectangular parallelepiped. For example, the peak intensities for the parallelepiped cloud are still below those of the cylindrical cloud with a larger volume. These results are consistent with experimental findings, since a dilute cloud is expected to provide less resistance to the propagation of the intensity of radiation.

To continue the comparison with [1], a modified cylinder of equal height and radius ($r = h = 7$ km) with a polar angle $\theta = 90^o$ is used. The volume of this modified cylinder is 1077.6 cubic kilometers, which is very close to the volume of the cubic cloud at 1000 cubic kilometers. We expect the peak intensity of this modified cylinder to be larger than that of the cubic cloud, and in fact it is ($I_{cubic} = 2.70\times10^{-14}$, $I_{cylinder} = 3.66\times10^{-12}$). See Figure 28 below.

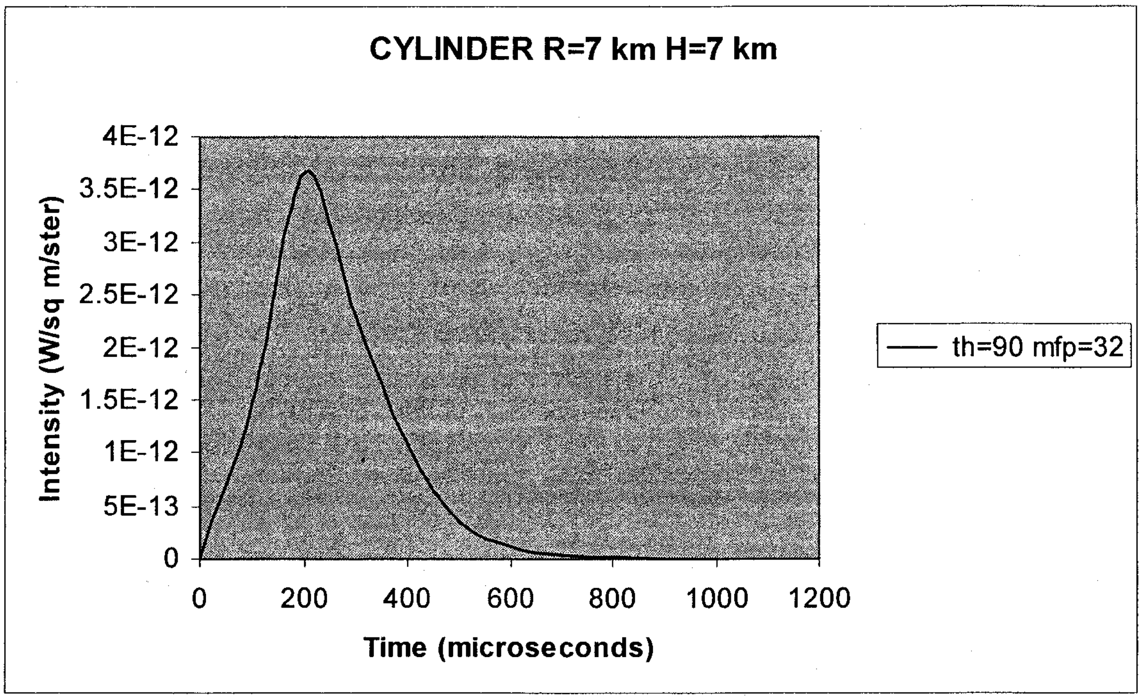

Figure 28

This observation is worthy to be singled out. Figure 23 represents the relationship between intensity and time at the ideal or the optimal position for the cubic cloud. The ideal point source is located at the center of the cloud and the detector is at or above the center of the cloud, looking down. On the other hand, Figure 28 displays the relationship between intensity and time at the optimal position for the cylindrical cloud. The polar angle is $\theta = 90^\circ$, the detector is located at the top corner of the cylinder and is looking down. The fact that the peak intensity of the propagation of radiation for the cylinder is higher than that of the cube is an indication that the cylinder represents a more conducive channel of propagation. This gives credence to the school of thought that the cylinder is the more natural geometry to model the cloud.

Moreover, from [2], we have Figure 29, which is provided below.

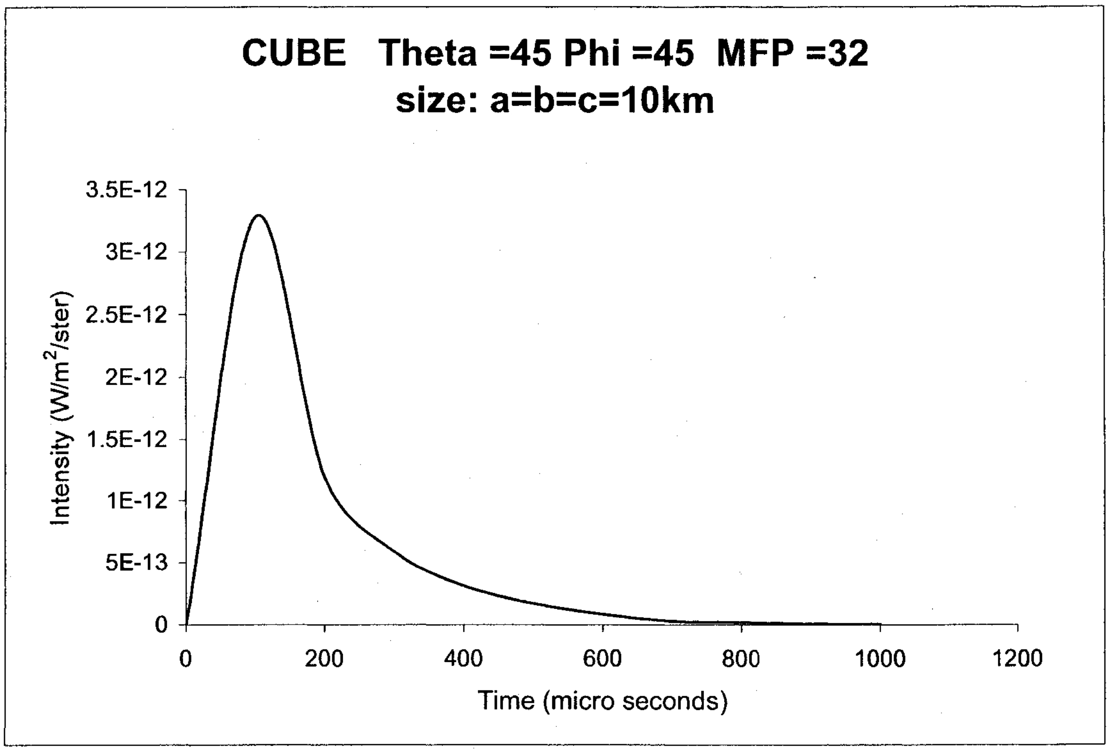

Figure 29

The peak intensity of the cube is near the peak intensity of the cylinder. The peak intensity for the cylinder is 3.66×10^{-12}, while the peak intensity for the cube is 3.40×10^{-12}. This near similarity of the two models is achieved when, for the cube, $\theta=45^o$, $\phi=45^o$, $K=32$. For the cylinder, its optimal position is $\theta=90^o$, $K=32$ and the point source is located at the top corner of the cylinder.

6.2 Future Work

Our discussion of future work will be developed along three tracks.

Track 1: Generalization of the operator $\mathcal{L}$ of equation (22).

The differential equation (22)

$$\lambda_i^2\Psi_i(\vec{r})=\mathcal{L}\Psi_i(\vec{r}), \qquad \vec{r}\in V;$$

$$\lambda_i^2(\vec{r})=0, \qquad \vec{r}\in S_{ext},$$

is quite general. The operator $\mathcal{L}=-\nabla\cdot[D(\vec{r})\cdot\nabla]+(1-\omega_0)K(\vec{r})c$ is very complicated. In this thesis, $D(\vec{r})$ was assumed to be constant in order to apply the diffusion approximation. In future work, numerical analysis will be used to approximate $D(\vec{r})$ or successive iteration will be utilized by assuming $D(\vec{r})\ \alpha\ r^n$, where n will have to be determined experimentally.

Track 2: The Use of Statistics

In our derivation, the cylindrical cloud was assumed to be composed of identical spherical water droplets. In the future, we will consider the medium to consist of an inhomogeneous distribution of non-identical scatterers. For example, the presence of ice particle, needle or crystal-shaped objects will be allowed to be present in the embedding medium. The formulation of the problem will use either stochastic analysis or spatial statistics in addition to pair-correlated random distribution functions. Typical examples of this type of cloud belong to the cirrus family.

Track 3: Multiple Scattering Approach

This effort will start from equation (23):

$$(\nabla^2 + k^2)\Psi'_i(\vec{r}) = 0,$$

$$k^2 = [\lambda_i^2 - (1-\omega_o)K(\vec{r})c]/D(\vec{r}).$$

The first part of the equation is a general form of the Helmholtz equation, which is the basis of the whole fabric of Twersky's scattering theory [23], [24], [25].

APPENDIX A

The purpose of this appendix is to provide readers with the necessary details involved in the derivation of equation (16) of [1] and equation (16) of Chapter 3 in cylindrical coordinates.

$$\lambda_i^2\Psi_i(\vec{r}) = \{-\nabla\cdot[D(\vec{r})\cdot\nabla] + (1-\omega_o)K(\vec{r})c\}\Psi_i(\vec{r}), \tag{A.1}$$

$$\lambda_i^2 + [D(\vec{r})\cdot\nabla^2] - (1-\omega_o)K(\vec{r})c\}\Psi_i(\vec{r}) = 0, \tag{A.2}$$

$$[\nabla^2 + \{(\lambda_i^2 - (1-\omega_o)K(\vec{r})c)/D(\vec{r})\}]\Psi_i(\vec{r}) = 0. \tag{A.3}$$

Equation (A.3) is in the form of a wave equation

$$(\nabla^2 + k^2)\Psi_i(\vec{r}) = 0, \quad \text{where } k^2 = [\lambda_i^2 - (1-\omega_o)K(\vec{r})c]/D(\vec{r}). \tag{A.4}$$

(A.4) is equation (23) of Chapter 4.

To continue, we introduce cylindrical coordinates and assume the solution is of the form

$$\Psi(\vec{r}) = \Psi(\rho,\theta,z) = R(\rho)\Theta(\theta)Z(z). \tag{A.5}$$

Substituting equation (A.1) into (A.4), we obtain

$$(\nabla^2 + k^2)R(\rho)\Theta(\theta)Z(z) = 0. \tag{A.6}$$

Using reference [21] and equation (A.6), we have

$$\frac{1}{\rho}\frac{\partial}{\partial\rho}(\rho\frac{\partial\Psi}{\partial\rho}) + \frac{1}{\rho^2}\frac{\partial^2\Psi}{\partial\theta^2} + \frac{\partial^2\Psi}{\partial z^2} + k^2\Psi = 0, \tag{A.7}$$

$$\frac{1}{\rho}\frac{\partial}{\partial\rho}(\rho\frac{\partial R\Theta Z}{\partial\rho}) + \frac{1}{\rho^2}\frac{\partial^2 R\Theta Z}{\partial\theta^2} + \frac{\partial^2 R\Theta Z}{\partial z^2} + k^2 R\Theta Z = 0. \tag{A.8}$$

Performing the operation in (A.8) leads to

$$\frac{\Theta Z}{\rho}\frac{d}{d\rho}(\rho\frac{dR}{d\rho})+\frac{RZ}{\rho^2}\frac{d^2\Theta}{d\theta^2}+\mathrm{P}\Theta\frac{d^2Z}{dz^2}+k^2R\Theta Z=0\,. \tag{A.9}$$

Dividing by $R\Theta Z$, we obtain

$$\frac{1}{R\rho}\frac{d}{d\rho}(\rho\frac{dR}{d\rho})+\frac{1}{\rho^2\Theta}\frac{d^2\Theta}{d\theta^2}+\frac{1}{Z}\frac{d^2Z}{dz^2}+k^2=0\,. \tag{A.10}$$

Isolating the z-term gives

$$\frac{1}{R\rho}\frac{d}{d\rho}(\rho\frac{dR}{d\rho})+\frac{1}{\rho^2\Theta}\frac{d^2\Theta}{d\theta^2}+k^2=-\frac{1}{Z}\frac{d^2Z}{dz^2}\,. \tag{A.11}$$

In order for this to be true, both sides of the equation must be equal to the same constant.

Firstly,

$$-\frac{1}{Z}\frac{d^2Z}{dz^2}=\gamma^2\,.$$

Thus,

$$\frac{d^2Z}{dz^2}+\gamma^2Z=0\,, \tag{A.12}$$

whose solution is

$$Z(z)=A_\gamma\sin\gamma z+B_\gamma\cos\gamma z\,. \tag{A.13}$$

Secondly,

$$\frac{1}{R\rho}\frac{d}{d\rho}(\rho\frac{dR}{d\rho})+\frac{1}{\rho^2\Theta}\frac{d^2\Theta}{d\theta^2}+k^2=\gamma^2\,. \tag{A.14}$$

Isolating the Θ term and multiplying by ρ^2, we have

$$\frac{\rho}{R}\frac{d}{d\rho}(\rho\frac{dR}{d\rho})+k^2\rho^2-\gamma^2\rho^2=-\frac{1}{\Theta}\frac{d^2\Theta}{d\theta^2}\,. \tag{A.15}$$

Choosing the constant in (A.15) to be m^2, we proceed as follows:

$$-\frac{1}{\Theta}\frac{d^2\Theta}{d\theta^2}=m^2,$$

$$\frac{d^2\Theta}{d\theta^2}+m^2\Theta=0. \tag{A.16}$$

The solution of (A.16) is then

$$\Theta(\theta)=A_m \sin m\theta+B_m \cos m\theta.$$

Finally, we consider the radial dependence segment of the derivation. Equating the radial part of (A.15) to the chosen m^2 used in (A.16) leads to

$$\frac{\rho}{R}\frac{d}{d\rho}(\rho\frac{dR}{d\rho})+k^2\rho^2-\gamma^2\rho^2=m^2 \quad \text{or} \quad \frac{\rho}{R}\frac{d}{d\rho}(\rho\frac{dR}{d\rho})+(k^2\rho^2-\gamma^2\rho^2)-m^2=0. \tag{A.17}$$

Let $k^2-\gamma^2=\alpha^2$, and multiply by R to obtain

$$\rho\frac{d}{d\rho}(\rho\frac{dR}{d\rho})+(\alpha^2\rho^2-m^2)R=0. \tag{A.18}$$

Using the product rule to expand the first term of (A.18), we have

$$\rho[\rho\cdot\frac{d^2R}{d\rho^2}+\frac{dR}{d\rho}\cdot 1]+(\alpha^2\rho^2-m^2)R=0, \text{ or}$$

$$\rho^2\cdot\frac{d^2R}{d\rho^2}+\rho\frac{dR}{d\rho}+(\alpha^2\rho^2-m^2)R=0. \tag{A.19}$$

Equation (A.19) is recognized as being part of the Bessel family of equations of order ν. The general form of the Bessel equation is given by reference [22] to be

$$q^2R''+qR'+(q^2-\nu^2)R=0. \tag{A.20}$$

To apply the Bessel equation in (A.20), a change of variables must be made.

Let $q=\alpha\rho$, or $\rho=\frac{q}{\alpha}$.

Firstly, we obtain $\frac{dR}{d\rho}=\frac{dR}{dq}\cdot\frac{dq}{d\rho}=\frac{dR}{d\rho}\cdot\alpha=\alpha\frac{dR}{d\rho}$; (A.21)

secondly, $\frac{d^2R}{d\rho^2}=\frac{d}{d\rho}(\frac{dR}{d\rho})=\alpha^2\frac{d^2R}{dq^2}$. (A.22)

Substituting (A.21) and (A.22) into (A.19) then yields

$$\frac{q}{\alpha^2}^2\cdot\alpha^2\frac{d^2R}{dq^2}+\frac{q}{\alpha}\cdot\alpha\frac{dR}{dq}+(q^2-m^2)R=0 \text{ or } q^2\frac{d^2R}{dq^2}+q\frac{dR}{dq}+(q^2-m^2)R=0. \quad (A.23)$$

Hence, equation (A.19) has been transformed into a Bessel equation of order m.

$$R(q)=A_mJ_m(q)+B_mY_m(q). \quad (A.24)$$

The solutions of (A.23) are the well known Bessel functions.

Replacing $q=\alpha\rho$ in (A.24) gives

$$R(\rho)=A_mJ_m(\alpha\rho)+B_mY_m(\alpha\rho). \quad (A.25)$$

Equation (A.25) is equation (30) of Chapter 4.

APPENDIX B

This appendix deals with parts (b) and (c) of Section 4.3. Part (b) is concerned with the evaluation of $\int_V \Psi^2_{lmn}(\vec{r})dV$ while part (c) is the derivation of $\hat{\Omega}\cdot\nabla\Psi_{lmn}$.

We begin with

$$\int_V \Psi^2_{lmn}(\vec{r})dV = \int_0^l\int_0^{2\pi}\int_0^a J_n^2(\frac{\chi_{nl}}{a}\rho)\sin^2(m\theta)\sin^2(\frac{n\pi}{L}z)\rho d\rho d\theta dz$$

$$= \int_0^a J_n^2(\frac{\chi_{nl}}{a}\rho)\rho d\rho\int_0^{2\pi}\sin^2(m\theta)d\theta\int_0^L\sin^2(\frac{n\pi}{L}z)dz$$

$$= \int_0^a [\frac{2}{\pi\frac{\chi_{nl}}{a}\rho}\cos^2(\frac{\chi_{nl}}{a}\rho-\frac{3\pi}{4})]\rho d\rho\int_0^{2\pi}\sin^2(m\theta)d\theta\int_0^L\sin^2(\frac{n\pi}{L}z)dz$$

$$= \frac{2a}{\pi\chi_{nl}}\int_0^a[\cos^2(\frac{\chi_{nl}}{a}\rho-\frac{3\pi}{4})]d\rho\int_0^{2\pi}\sin^2(m\theta)d\theta\int_0^L\sin^2(\frac{n\pi}{L}z)dz\,. \qquad \text{(B.1)}$$

I II III

To facilitate the derivations, equation (B.1) is divided into three parts (I, II, and III). Each part will be dealt with separately.

We begin with Part I:

$$\text{I} = \frac{2a}{\pi\chi_{nl}}\int_0^a[\cos^2(\frac{\chi_{nl}}{a}\rho-\frac{3\pi}{4})]d\rho \quad = \quad \frac{2a}{\pi\chi_{nl}}\int_0^a[\cos^2(\frac{\chi_{nl}}{a}\rho-\frac{3\pi}{4})]d\rho\,. \qquad \text{(B.2)}$$

Using the trigonometric identity $\cos^2(ax+b)=\frac{1}{2}[\cos 2(ax+b)+1]$ in (B.2) leads to

$$\mathrm{I} = \frac{2a}{\pi\chi_{nl}}\int_0^a \frac{1}{2}[\cos 2(\frac{\chi_{nl}}{a}\rho - \frac{3\pi}{4}) + 1]d\rho = \frac{a}{\pi\chi_{nl}}[\frac{a}{2\chi_{nl}}\frac{1}{2}\sin 2(\frac{\chi_{nl}}{a}\rho - \frac{3\pi}{4}) + \rho]\Big|_0^a$$

$$= \frac{a}{\pi\chi_{nl}}[\frac{a}{2\chi_{nl}}\sin 2(\frac{\chi_{nl}}{a}a - \frac{3\pi}{4}) + a] - [\frac{a}{2\chi_{nl}}\sin 2(\frac{\chi_{nl}}{a}0 - \frac{3\pi}{4}) + 0]$$

$$= \frac{a}{\pi\chi_{nl}}[\frac{a}{2\chi_{nl}}\sin 2(\chi_{nl} - \frac{3\pi}{4}) + a] - [\frac{a}{2\chi_{nl}}\sin 2(-\frac{3\pi}{4})]. \qquad \text{(B.3)}$$

Continuing with the simplification of equation (B.3) gives

$$\mathrm{I} = \frac{a}{\pi\chi_{nl}}[\frac{a}{2\chi_{nl}}\sin 2(\chi_{nl} - \frac{3\pi}{4}) + a] + [\frac{a}{2\chi_{nl}}\sin(\frac{3\pi}{2})]$$

$$= \frac{a}{\pi\chi_{nl}}[\frac{a}{2\chi_{nl}}\sin 2(\chi_{nl} - \frac{3\pi}{4}) + a - \frac{a}{2\chi_{nl}}] = \frac{a}{\pi\chi_{nl}}\cdot\frac{a}{2\chi_{nl}}[\sin(\chi_{nl} - \frac{3\pi}{4}) + 2\chi_{nl} - 1]$$

$$= \frac{a^2}{2\pi\chi_{nl}{}^2}[\sin(\chi_{nl} - \frac{3\pi}{4}) + 2\chi_{nl} - 1] \quad = \quad \frac{2a}{\pi\frac{\chi_{nl}}{a}}\int_0^a [J_n^2(\frac{\chi_{nl}}{a})]d\rho. \qquad \text{(B.4)}$$

The evaluation of parts II and part III are straightforward. They are provided here for the sake of completeness.

$$\mathrm{II} = \int_0^{2\pi}\sin^2(m\theta)d\theta \quad = \int_0^{2\pi}\frac{1}{2}[1 - \cos(2m\theta)]d\theta = \frac{1}{2}[\theta - \frac{1}{2m}\sin 2m\theta]\Big|_0^{2\pi}$$

$$= \frac{1}{2}[2\pi - \frac{1}{2m}\sin 2m2\pi] - [0 - \frac{1}{2m}\sin 2m(0)] = \frac{1}{2}[2\pi] \quad = \quad \pi. \qquad \text{(B.5)}$$

$$\mathrm{III} = \int_0^L \sin^2(\frac{n\pi}{L}z)dz \quad = \int_0^L \frac{1}{2}[1 - \cos(\frac{2n\pi}{L}z)]dz = \frac{1}{2}[z - \frac{1}{2n\pi}\sin(\frac{2n\pi}{L}z)]\Big|_0^L$$

$$= \frac{1}{2}[L - \frac{L}{2n\pi}\sin(\frac{2n\pi}{L}\cdot L)] - [0 - \frac{L}{2n\pi}\sin(2n\pi\cdot 0)] \; = \; \frac{L}{2}. \qquad \text{(B.6)}$$

Combining the results of (B.4), (B.5), and (B.6) gives

$$\int_V \Psi^2_{lmn}(\vec{r})dV = \int_0^l \int_0^{2\pi} \int_0^a J_n^2(\frac{\chi_{nl}}{a}\rho)\sin(m\theta)\sin(\frac{n\pi}{L}z)\rho d\rho d\theta dz$$

$$=\frac{a^2}{2\pi\chi_{nl}{}^2}[\sin(\chi_{nl}-\frac{3\pi}{4})+2\chi_{nl}-1]\cdot\pi\cdot\frac{L}{2}=\frac{a^2}{4\chi_{nl}{}^2}[\sin(\chi_{nl}-\frac{3\pi}{4})+2\chi_{nl}-1]$$

$$=(\frac{a}{2\chi_{nl}})^2[\sin(\chi_{nl}-\frac{3\pi}{4})+2\chi_{nl}-1]. \tag{B.7}$$

Evaluation of $\hat{\Omega}\cdot\nabla\Psi_{lmn}$:

Start with

$$\Psi_{lmn}(\vec{r}) = J_n(\frac{\chi_{nl}}{a}\rho)\sin(m\theta)\sin(\frac{n\pi}{L}z).$$

From [21], the above equation is approximated as follows:

$$\Psi_{lmn}(\vec{r}) \approx \sqrt{\frac{2}{\pi\frac{\chi_{nl}}{a}\rho}}\cos(\frac{\chi_{nl}}{a}\rho-\frac{3\pi}{4})\sin(m\theta)\sin(\frac{n\pi}{L}z) .$$

Since the unit vector in cylindrical coordinates is

$$\hat{\Omega} = \hat{x}\sin\theta\cos\phi + \hat{y}\sin\theta\sin\phi + \hat{z}\cos\theta,$$

the gradient operator in cylindrical coordinates is, from [21],

$$\nabla \equiv \frac{\partial}{\partial\rho}\hat{\rho} + \frac{1}{\rho}\frac{\partial}{\partial\theta}\hat{\theta} + \frac{\partial}{\partial z}\hat{z}.$$

We then have

$$\frac{\partial}{\partial\rho}\Psi_{lmn}(\vec{r}) = [\frac{\partial}{\partial\rho}J_n(\frac{\chi_{nl}}{a}\rho)]\sin(m\theta)\sin(\frac{n\pi}{L}z)$$

$$=[\frac{\partial}{\partial\rho}\sqrt{\frac{2}{\pi\frac{\chi_{nl}}{a}\rho}}\cos(\frac{\chi_{nl}}{a}\rho-\frac{3\pi}{4})]\sin(m\theta)\sin(\frac{n\pi}{L}z). \tag{B.8}$$

Continuing with the simplification of (B.8), we obtain

$$\frac{\partial}{\partial\rho}\Psi_{lmn}(\vec{r}) = [\frac{\partial}{\partial\rho}(\sqrt{\frac{2a}{\pi\chi_{nl}}}\rho^{-\frac{1}{2}}\cdot\cos(\frac{\chi_{nl}}{a}\rho-\frac{3\pi}{4}))]\sin(m\theta)\sin(\frac{n\pi}{L}z)$$

$$=\{[\sqrt{\frac{2a}{\pi\chi_{nl}}}\rho^{-\frac{1}{2}}]\cdot[\frac{\chi_{nl}}{a}\sin(\frac{\chi_{nl}}{a}\rho-\frac{3\pi}{4})]+$$

$$[\sqrt{\frac{2a}{\pi\chi_{nl}}}\cos(\frac{\chi_{nl}}{a}\rho-\frac{3\pi}{4})]\cdot[-\frac{1}{2}\rho^{-\frac{3}{2}}]\}\sin(m\theta)\sin(\frac{n\pi}{L}z)$$

$$=\{[-\sqrt{\frac{2a}{\pi\chi_{nl}}}\rho^{-\frac{1}{2}}]\cdot[\frac{\chi_{nl}}{a}\sin(\frac{\chi_{nl}}{a}\rho-\frac{3\pi}{4})]+\frac{1}{2\rho}\cos(\frac{\chi_{nl}}{a}\rho-\frac{3\pi}{4})]\}\sin(m\theta)\sin(\frac{n\pi}{L}z)$$

$$=\{[-\sqrt{\frac{2a}{\pi\chi_{nl}}}\frac{1}{\rho^{\frac{1}{2}}}]\cdot[\frac{\chi_{nl}}{a}\sin(\frac{\chi_{nl}}{a}\rho-\frac{3\pi}{4})]+\frac{1}{2\rho}\cos(\frac{\chi_{nl}}{a}\rho-\frac{3\pi}{4})]\}\sin(m\theta)\sin(\frac{n\pi}{L}z)$$

$$=-\sqrt{\frac{2a}{\pi\chi_{nl}\rho}}[\frac{\chi_{nl}}{a}\sin(\frac{\chi_{nl}}{a}\rho-\frac{3\pi}{4})]+\frac{1}{2\rho}\cos(\frac{\chi_{nl}}{a}\rho-\frac{3\pi}{4})]\sin(m\theta)\sin(\frac{n\pi}{L}z). \qquad \text{(B.9)}$$

Now, consider the contribution of the third term of the gradient operator applied to the eigenfunctions Ψ_{lmn}:

$$\frac{1}{\rho}\frac{\partial}{\partial\theta}\Psi_{lmn}(\vec{r}) = J_n(\frac{\chi_{nl}}{a}\rho)[\frac{\partial}{\partial\theta}\sin(m\theta)]\sin(\frac{n\pi}{L}z)$$

$$=\frac{1}{\rho}[\frac{\partial}{\partial\theta}\sin(m\theta)]J_n(\frac{\chi_{nl}}{a}\rho)\sin(\frac{n\pi}{L}z)$$

$$=\frac{1}{\rho}[m\cos m\theta)]J_n(\frac{\chi_{nl}}{a}\rho)\sin(\frac{n\pi}{L}z). \qquad \text{(B.10)}$$

Using the trigonometric function of $J_n(\frac{\chi_{nl}}{a}\rho)$ in (B.10), we obtain

$$\frac{1}{\rho}\frac{\partial}{\partial\theta}\Psi_{lmn}(\vec{r}) = \frac{m}{\rho}[\cos m\theta)]\cdot\sqrt{\frac{2a}{\pi\chi_{nl}\rho}}\cos(\frac{\chi_{nl}}{a}\rho-\frac{3\pi}{4})\cdot\sin(\frac{n\pi}{L}z). \qquad \text{(B.11)}$$

Finally, with the z-component of the gradient operator we have

$$\frac{\partial}{\partial z}\Psi_{lmn}(\vec{r}) = J_n(\frac{\chi_{nl}}{a}\rho)\sin(m\theta)[\frac{\partial}{\partial z}\sin(\frac{n\pi}{L}z)] = [\frac{\partial}{\partial z}\sin(\frac{n\pi}{L}z)]J_n(\frac{\chi_{nl}}{a}\rho)\sin(m\theta)$$

$$=[\frac{n\pi}{L}\cos(\frac{n\pi}{L}z)]J_n(\frac{\chi_{nl}}{a}\rho)\sin(m\theta)$$

$$=\frac{n\pi}{L}\cos(\frac{n\pi}{L}z)\sin(m\theta)\sqrt{\frac{2a}{\pi\chi_{nl}\rho}}\cos(\frac{\chi_{nl}}{a}\rho-\frac{3\pi}{4}). \qquad \text{(B.12)}$$

Combining equations (B.8), (B.11), and (B.12) together gives

$$\nabla\Psi_{lmn} = \frac{\partial}{\partial\rho}\Psi_{lmn}(\vec{r})\hat{\rho} + \frac{1}{\rho}\frac{\partial}{\partial\theta}\Psi_{lmn}(\vec{r})\hat{\theta} + \frac{\partial}{\partial z}\Psi_{lmn}(\vec{r})\hat{z}$$

$$=\{[-\sqrt{\frac{2a}{\pi\chi_{nl}\rho}}[\frac{\chi_{nl}}{a}\sin(\frac{\chi_{nl}}{a}\rho-\frac{3\pi}{4})]+\frac{1}{2\rho}\cos(\frac{\chi_{nl}}{a}\rho-\frac{3\pi}{4})]\sin(m\theta)\sin(\frac{n\pi}{L}z)\}\,\hat{\rho}$$

$$+\{\frac{m}{\rho}[\cos m\theta)]\cdot J_n(\frac{\chi_{nl}}{a}\rho)\cdot\sin(\frac{n\pi}{L}z)\}\,\hat{\theta}$$

$$+\{\frac{n\pi}{L}\cos(\frac{n\pi}{L}z)\sin(m\theta)J_n(\frac{\chi_{nl}}{a}\rho)\}\,\hat{z}. \qquad \text{(B.13)}$$

Using the approximation of the Bessel function of the first kind J of order n=1 leads to the result

$$\nabla\Psi_{lmn} = \{[-\sqrt{\frac{2a}{\pi\chi_{nl}\rho}}[\frac{\chi_{nl}}{a}\sin(\frac{\chi_{nl}}{a}\rho-\frac{3\pi}{4})]+\frac{1}{2\rho}\cos(\frac{\chi_{nl}}{a}\rho-\frac{3\pi}{4})]\sin(m\theta)\sin(\frac{n\pi}{L}z)\}\,\hat{\rho}$$

$$+\{\frac{m}{\rho}[\cos m\theta)]\cdot\sqrt{\frac{2a}{\pi\chi_{nl}\rho}}\cos(\frac{\chi_{nl}}{a}\rho-\frac{3\pi}{4})\cdot\sin(\frac{n\pi}{L}z)\}\,\hat{\theta}$$

$$+\{\frac{n\pi}{L}\cos(\frac{n\pi}{L}z)\sin(m\theta)\sqrt{\frac{2a}{\pi\chi_{nl}\rho}}\cos(\frac{\chi_{nl}}{a}\rho-\frac{3\pi}{4})\}\,\hat{z}. \qquad \text{(B.14)}$$

Next, we consider the relationship between the Cartesian unit vectors and the cylindrical unit vectors.

Starting with

$$\begin{bmatrix} \hat{\rho} \\ \hat{\theta} \\ \hat{z} \end{bmatrix} = \begin{bmatrix} \cos\theta & \sin\theta & 0 \\ -\sin\theta & \cos\theta & 0 \\ 0 & 0 & 1 \end{bmatrix} \begin{bmatrix} \hat{x} \\ \hat{y} \\ \hat{z} \end{bmatrix} \tag{B.15}$$

from reference [22], we have

$\hat{\rho} = \hat{x}\cos\theta + \hat{y}\sin\theta$

$\hat{\theta} = -\hat{x}\sin\theta + y\cos\theta$

$\hat{z} = \hat{z}$.

The unit vector $\hat{\Omega}$ given by [1],

$\hat{\Omega} = \hat{x}\sin\theta\cos\phi + \hat{y}\sin\theta\sin\phi + \hat{z}\cos\theta$, is transformed into

$\hat{\Omega} = \sin\theta(\hat{x}\cos\phi + \hat{y}\sin\phi) + \hat{z}\cos\theta$, which becomes

$\hat{\Omega} = \hat{\rho}\sin\theta + \hat{z}\cos\theta$ (there is no ϕ term).

Therefore, combining all the above gives the desired result:

$\hat{\Omega}\cdot\nabla\Psi_{lmn} =$

$$\{[-\sqrt{\frac{2a}{\pi\chi_{nl}\rho}}[\frac{\chi_{nl}}{a}\sin(\frac{\chi_{nl}}{a}\rho - \frac{3\pi}{4})] + \frac{1}{2\rho}\cos(\frac{\chi_{nl}}{a}\rho - \frac{3\pi}{4})]\sin(m\theta)\sin(\frac{n\pi}{L}z)\cdot\sin\theta\}$$

$$+\{\frac{n\pi}{L}\cos(\frac{n\pi}{L}z)\sin(m\theta)\sqrt{\frac{2a}{\pi\chi_{nl}\rho}}\cos(\frac{\chi_{nl}}{a}\rho - \frac{3\pi}{4})\cdot\cos\theta\}. \tag{B.16}$$

Finally, the intensity distribution in cylindrical coordinates is given by

$$I(\vec{r},\hat{\Omega},t)=\frac{\chi_{ln}^{2}}{a^{2}\pi L\cdot[\sin(\chi_{ln}-\frac{3\pi}{4})+2\chi_{ln}-1]}\cdot$$

$$\sum_{l=1}^{\infty}\sum_{m=1}^{\infty}\sum_{n=1}^{\infty}\Psi_{lmn}(\vec{r})-\frac{3D}{c}\hat{\Omega}\cdot\nabla\Psi_{lmn}(\vec{r})][\sum_{j=1}^{N}\omega_{j}\Psi_{lmn}(\vec{r}_{j})e^{-\lambda_{lmn}^{2}(t-t_{j})}]. \qquad \text{(B.17)}$$

Substituting (B.16) into (B.17) produces

$$I(\vec{r},\hat{\Omega},t)=\frac{\chi_{ln}^{2}}{a^{2}\pi L\cdot[\sin(\chi_{ln}-\frac{3\pi}{4})+2\chi_{ln}-1]}\cdot\sum_{l=1}^{\infty}\sum_{m=1}^{\infty}\sum_{n=1}^{\infty}J_{n}(\frac{\chi_{ln}}{a}\rho)\sin(n\theta)\sin(\frac{m\pi}{L}z)-\frac{3D}{c}\cdot$$

$$\{[-\sqrt{\frac{2a}{\pi\chi_{ln}\rho}}[\frac{\chi_{ln}}{a}\sin(\frac{\chi_{ln}}{a}\rho-\frac{3\pi}{4})]+\frac{1}{2\rho}\cos(\frac{\chi_{ln}}{a}\rho-\frac{3\pi}{4})]\sin(m\theta)\sin(\frac{n\pi}{L}z)\cdot\sin\theta\}+$$

$$\{\frac{n\pi}{L}\cos(\frac{n\pi}{L}z)\sin(m\theta)\sqrt{\frac{2a}{\pi\chi_{ln}\rho}}\cos(\frac{\chi_{ln}}{a}\rho-\frac{3\pi}{4})\cdot\cos\theta\}\cdot[\sum_{j=1}^{N}\omega_{j}\Psi_{lmn}(\vec{r}_{j})e^{-\lambda_{lmn}^{2}(t-t_{j})}]. \qquad \text{(B.18)}$$

After additional simplification, (B.18) is reduced to

$$I(\vec{r},\hat{\Omega},t)=\frac{\chi_{ln}^{2}}{a^{2}\pi L\cdot[\sin(\chi_{ln}-\frac{3\pi}{4})+2\chi_{ln}-1]}\cdot$$

$$\sum_{l=1}^{\infty}\sum_{m=1}^{\infty}\sum_{n=1}^{\infty}[\sqrt{\frac{2}{\pi\frac{\chi_{ln}}{a}\rho}}\cos(\frac{\chi_{ln}}{a}\rho-\frac{3\pi}{4})]\sin(n\theta)\sin(\frac{m\pi}{L}z)-\frac{3D}{c}\cdot$$

$$\{[-\sqrt{\frac{2a}{\pi\chi_{ln}\rho}}[\frac{\chi_{ln}}{a}\sin(\frac{\chi_{ln}}{a}\rho-\frac{3\pi}{4})]+\frac{1}{2\rho}\cos(\frac{\chi_{ln}}{a}\rho-\frac{3\pi}{4})]\sin(m\theta)\sin(\frac{n\pi}{L}z)\cdot\sin\theta\}+$$

$$\{\frac{n\pi}{L}\cos(\frac{n\pi}{L}z)\sin(m\theta)\sqrt{\frac{2a}{\pi\chi_{ln}\rho}}\cos(\frac{\chi_{ln}}{a}\rho-\frac{3\pi}{4})\cdot\cos\theta\}\cdot[\sum_{j=1}^{N}\omega_{j}\Psi_{lmn}(\vec{r}_{j})e^{-\lambda_{lmn}^{2}(t-t_{j})}], \qquad \text{(B.19)}$$

which provides the equation used for the intensity in this research.

REFERENCES

[1] Koshak, W. J., R. J. Solakiewicz, D. D. Phanord, and R. J. Blakeslee, Diffusion Model for Lightning Radiative Transfer, J. Geophysics.Res., Vol. 99, pp.14361-14371, 1994.

[2] Odei, J.B., Diffusion Model for Lightning Radiative Transfer Using Spherical Geometry, Masters Thesis, UNLV, August 2007.

[3] Thomason, L.W., and E.P. Krider, The Effects of Clouds on the Light Produced by Lightning, J. Atmos. Sci., 39, pp.2051-2065, 1982.

[4] Uman, M. A., The Lightning Discharge, pp.1-30, Academic Press, CA, 1987.

[5] Marshak, A. and A. B. Davis, 3D Radiative Transfer in Cloudy Atmospheres, pg. 7, Springer, NY, 2005.

[6] Schonland, B. F. J., Atmospheric Electricity, John Wiley & Sons, N.Y., 1953.

[7] Berger, K., R. B. Anderson and H Kroninger, Parameters of Lightning Flashes, Electra, 80, pp.23-27, 1975.

[8] Berger, K., Blitzsheom-Parameter von Augwartsblitzen, Bull. Schwiez. Elektrotech. Ver. 69: 353-360, 1978.

[9] Krider, E.P., Physics of Lightning, Studies in Geophysics, The Earth's Electrical Environment, pp. 30-40, National Academy Press, Washington, D.C. 1986.

[10] Lightning and the Space Program, NASA Facts, JFK Space Center, FL., FS-2005-10-031-KSC, Rev. 2006.

[11] Goody, R.M. and Y. L. Yung, Atmospheric Radiation – Theoretical Basis, 2nd Edition, pp. 5-14, Oxford University Press, 1989.

[12] Zhang, R., T. Xuexi and D. W. Bond, Impacts of Anthropogenic and Natural NO_x Sources Over the U.S. on Tropospheric Chemistry, Proceeding of the National Academy of Sciences, Vol. 100, No. 4, pp. 1505-1509, 2003.

[13] Chameides, W. L., The Role of Lightning in the Chemistry of the Atmosphere, Studies in Geophysics, The Earth's Electrical Environment, pp. 70-77, National Academy Press, Washington D.C., 1986.

[14] McCarthy, L. NASA Study Predicts More Severe Storms with Global Warming, August, 2007.

[15] Cook-Anderson, G., New Faraway Sensors Warn of Emerging Hurricane's Strength, September, 2007.

[16] Christian, H.J., R.J. Blakeslee, D.J. Boccipio, W.J. Koshak, S.J. Goodman and D. M. Mach, Science Data Validation Plan for the Lightning Imaging Sensor, George C. Marshall Space Flight Center Science Directorate, pp.1-29, 2000.

[17] Chisholm, W. A. and K. L. Cummins, On the Use of LIS/OTD Flash Density in Electric Utility Reliability Analysis, August, 2006.

[18] Arfken, G., Mathematical Methods for Physicists (1st ed.), pp. 29, New York, 1966.

[19] Williams, M. M. R., Mathematical Methods in Particle Transport Theory, Ch. 11, John Wiley, 1971.

[20] Duderstadt, J. J., and W. R. Martin, Transport Theory, pp. 139, John Wiley & Sons, New York, 1979.

[21] Arfken, G. B., and H. J. Weber, Mathematical Methods for Physicists (6th ed.), Section 2.4 and p. 723, Academic Press Inc., London, 2005.

[22] Zill, D.G., and M.R. Cullin, Advanced Engineering Mathematics (3rd edition), pp. 262-265, Jones and Bartlett Publishers, MA., 2006.

[23] Twersky ,V., On Scattering of Waves by Random Distributions, I. Free-Space Scatterer Formalism, Journal of Mathematical Physics, Vol. 3, No 4, pp. 700-715, July – August, 1962.

[24] Twersky ,V., On Scattering of Waves by Random Distributions, II. Two-Space Scatterer Formalism, Journal of Mathematical Physics, Vol. 3, No 4, pp. 724-734, July – August, 1962.

[25] Twersky ,V., On a General Class of Scattering Problems, Journal of Mathematical Physics, Vol. 3, No 4, July – August, 1962.

VITA

Graduate College
University of Nevada, Las Vegas

Rina Alfonso Santos

Local Address:
4724 Laurentia Avenue,
Las Vegas, NV 89141

Degrees:
Associate of Science, Mathematics, 1986
College of Alameda, California

Bachelor of Science, Mathematics, 1993,
California State University, Hayward

Special Award:
Women's Mathematics Award

Thesis title:
A Diffusion Model of Lightning Radiative Transfer Using Cylindrical Geometry

Thesis Examination Committee:
Chairperson, Dr. Dieudonne Phanord, Ph.D.
Committee Member, Dr. Zhonghai Ding, Ph.D.
Committee Member, Dr. Rohan Dalpatadu, Ph.D.
Graduate Faculty Representative, Dr. Michael Pravica, Ph.D.